

Experimental characterization of Hall thruster breathing mode dynamics

Cite as: J. Appl. Phys. **130**, 133302 (2021); <https://doi.org/10.1063/5.0046048>

Submitted: 31 January 2021 . Accepted: 10 September 2021 . Published Online: 04 October 2021

 Ethan T. Dale and Benjamin A. Jorns

COLLECTIONS

Paper published as part of the special topic on [Physics of Electric Propulsion](#)



View Online



Export Citation



CrossMark

ARTICLES YOU MAY BE INTERESTED IN

[Dual mode operation of a hydromagnetic plasma thruster to achieve tunable thrust and specific impulse](#)

Journal of Applied Physics **130**, 133301 (2021); <https://doi.org/10.1063/5.0051467>

[Hydrodynamics of fringing-field induced defects in nematic liquid crystals](#)

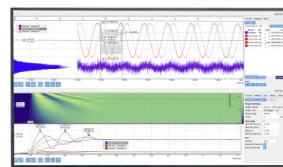
Journal of Applied Physics **130**, 134701 (2021); <https://doi.org/10.1063/5.0062532>

[Ion energy distribution function in very high frequency capacitive discharges excited by saw-tooth waveform](#)

Physics of Plasmas **28**, 103502 (2021); <https://doi.org/10.1063/5.0061605>

Challenge us.

What are your needs for
periodic signal detection?



Zurich
Instruments



Experimental characterization of Hall thruster breathing mode dynamics

Cite as: J. Appl. Phys. **130**, 133302 (2021); doi: [10.1063/5.0046048](https://doi.org/10.1063/5.0046048)

Submitted: 31 January 2021 · Accepted: 10 September 2021 ·

Published Online: 4 October 2021



View Online



Export Citation



CrossMark

Ethan T. Dale^{a)}  and Benjamin A. Jorns

AFFILIATIONS

Department of Aerospace Engineering, University of Michigan, Ann Arbor, Michigan 48109, USA

Note: This paper is part of the Special Topic on Physics of Electric Propulsion.

^{a)}Author to whom correspondence should be addressed: etdale@umich.edu

ABSTRACT

The dynamic properties of the Hall thruster breathing mode are investigated experimentally. Non-invasive time-resolved laser diagnostics are combined with a quasi-one-dimensional non-Maxwellian modeling technique to yield the high-speed evolution of a variety of plasma properties over the course of a breathing oscillation. The fluctuations of both ion and neutral densities are quantified in terms of amplitude and dispersion and are interpreted in the context of a simplified dispersion relation. It is found that the oscillations associated with the breathing mode are likely ion and neutral waves propagating with phase velocities commensurate with the local species drift speed. Further, the amplitudes of the waves are shown to decay with distance from the anode. This effect can be explained largely by the influence of the expansion of the background plasma and neutral gas. This monotonic decay combined with the downstream propagating nature of the waves suggests that these oscillations are influenced by conditions upstream of the acceleration and ionization regions. By comparing the presence of these waves to inferred electron temperature fluctuations, the hypothesis that the breathing mode is governed by a process in which the modulation of the neutral density near the anode sheath or the anode itself is coupled to a downstream ionization instability is qualitatively explored. The possibility of these waves relating to cyclical recombination of ions at the anode is also discussed.

Published under an exclusive license by AIP Publishing. <https://doi.org/10.1063/5.0046048>

I. INTRODUCTION

Hall thrusters are an enabling form of electric propulsion technology currently used in near-Earth applications and baselined for a number of upcoming deep space missions.^{1,2} Despite this high level of maturity, however, there are aspects of Hall thruster operation that remain poorly understood. Most notably, these devices exhibit several plasma instabilities,³ where the processes governing the onset and transition between some of these modes are not well characterized.

Hall thrusters support a wide range of instabilities because the mechanisms underlying the fundamental operation of the thruster give rise to several energy sources for wave growth. These devices consist of an annular channel, open to vacuum at the downstream side (the “exit plane”). A radial magnetic field is applied across the channel near the exit plane while an axial electric field is applied from an upstream annular anode to a downstream cathode mounted near the thruster exit. During operation, neutral gas is injected from the anode and rapidly ionized inside the channel in a location termed the “ionization region.” The heavier species that

result from this ionization, the ions, are relatively unmagnetized and accelerated out of the device by the applied electric field. The spatial location where the ion velocity increases is called the “acceleration zone.” The lighter, magnetized electrons are largely trapped in the acceleration region in a high speed $E \times B$ drift, the so-called Hall current. The overlap of the ionization and acceleration regions combined with the crossed field configuration of electric and magnetic fields leads to strong gradients in density, velocity, and temperature; anisotropies in plasma properties and transport based on the magnetic field topography; and complex material interactions that can globally influence the performance of the thruster. All of these effects, in turn, can serve as potential energy sources that promote the growth of instabilities.³

One of the most prominent instabilities in Hall thrusters is the “breathing mode.” This mode is characterized by coherent low-frequency ($f_b \sim 10$ kHz) discharge current oscillations that are correlated with strong longitudinal fluctuations in the discharge plasma.^{4–7} These large amplitude oscillations have been shown to adversely impact performance in certain operating conditions.^{8–16}

The breathing mode is nearly ubiquitous in Hall thruster designs and as such has been the subject of many numerical and analytical studies over the past several decades.^{4,17–21} While there is an emerging consensus that the breathing mode is likely related to ionization in the thruster discharge, there remain a number of open questions as to why these ionization modes spontaneously arise—their energy source—and how they propagate in the plasma once they form—their dispersion. Possible mechanisms that have been proposed to address these questions include charged species recombination at the anode,²² electron diffusion in the discharge^{23,24} and near the anode,²⁵ and other aspects of electron energy evolution.²⁶ It remains unclear, however, as to which of these proposed mechanisms actually explains this instability.

While experimental validation ultimately is necessary for differentiating the hypotheses for the breathing mode, generating the required measurements for full validation has posed a challenge to date. It is typical (cf. Ref. 27) to use a global metric of the thruster operation such as oscillations in the discharge current for validating models. In this approach, experimental measurements of frequency and amplitude of the current oscillations are compared to model predictions. While this approach provides an expedient tool for comparison—discharge current measurements are relatively simple to measure in a Hall thruster—it invites a potential problem of uniqueness. Indeed, many of the models and theories that have been developed to date produce results that compare favorably to experiments in the magnitude and frequency of discharge current oscillations.^{4,19,28,29} And yet, although the models largely agree on this global metric, the underlying hypotheses for why these oscillations arise vary. In order to elucidate the validity of the physics underlying the actual process, there is a pressing need for measurements not only globally but also locally, i.e., of the dynamics of the plasma properties inside the acceleration and ionization zones. Characterizing the relative amplitudes and phases of the local plasma properties associated with the breathing mode would provide crucial data for validating and potentially refining existing theories.

The technical gap in validation data in large part stems from the difficulties in measuring time-resolved (TR) local plasma properties in the upstream regions of the thruster where the mode is believed to originate. Indeed, while there has been extensive experimental interrogation of the instability—including sensitivity

studies,³⁰ performance correlations using near-field probes and high-speed imaging,^{7,31} far-field plume measurements,^{32–34} and even some non-invasive internal tomography³⁵—most of these measurements have been performed downstream of the ionization zone. The relative dearth of data in the upstream region stems in part from the fact that conventional electrostatic probing techniques in this highly dynamic area can substantially perturb the plasma state.^{36,37} In order to advance the understanding of this phenomenon, the need is apparent to characterize the oscillation experimentally in these previously inaccessible regions. To this end, we employ in this investigation a novel analytical approach combined with a well-established diagnostic technique to non-invasively determine the time-resolved ion, electron, and neutral properties throughout the thruster channel.

This paper is organized in the following way. In Secs. II and III, we describe the experimental conditions under which we applied this technique and review the theoretical and practical aspects of the diagnostic. In Sec. IV, we present the data collected. Finally, in Sec. V, we discuss the dispersion and possible physical mechanisms correlated with the breathing mode.

II. EXPERIMENTAL SETUP

We conducted our experimental investigation in the Large Vacuum Test Facility (LVTF) at the University of Michigan. The LVTF is a 6-m diameter, 9-m long cryogenically pumped stainless steel-clad vacuum vessel capable of a measured pumping speed between 500 and 600 kl/s on xenon.³⁸ We employed the H9, a 9-kW magnetically shielded Hall effect thruster shown in Fig. 1, for our investigation. This device was designed jointly by the Jet Propulsion Laboratory, the Air Force Research Laboratory, and the University of Michigan. The design and performance of this thruster are detailed in Refs. 39 and 40. In the present work, the H9 was operated at 300 V and 3 kW with a magnetic field strength of 75% the nominal value and a centrally mounted cathode with a 7% flow fraction. The facility pressure as measured per the recommended standard⁴¹ in the plane of the thruster was $\sim 4\mu\text{Torr-Xe}$. The thruster body was maintained at cathode potential to keep the thruster circuit isolated from the ground and to prevent the body from floating too negative and experiencing excessive erosion, based on the study of Ref. 42. The thruster was run consistently in

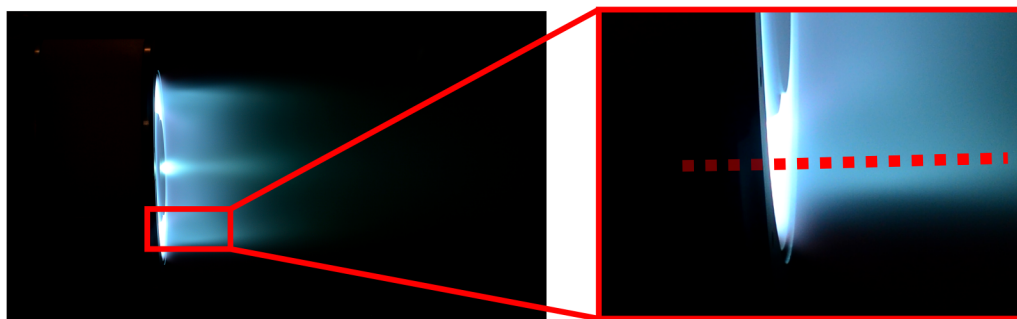


FIG. 1. Photograph of the H9 firing in the LVTF at 300 V and 3 kW with an inset notionally depicting the measurement domain.

this manner as it is expected that the breathing mode is sensitive to the electrical configuration.⁴²

III. METHODOLOGY

As outlined in Sec. I, we are ultimately interested in measuring the time-resolved behavior of key local plasma properties correlated with the breathing mode such as the relative phase and amplitude of plasma density as it evolves throughout the discharge. To this end, we describe in Sec. III A the methodology we employed to make these measurements non-invasively. We first outline the parameters of the primary diagnostic, laser-induced fluorescence (LIF), and then discuss our analysis approach for relating LIF measurements to local plasma properties.

A. Laser-induced fluorescence

The primary diagnostic tool we used in this study was LIF, which yielded both time-averaged (TA) and time-resolved (TR) measurements of the ion and neutral velocity distribution functions (VDFs) along the channel centerline of the H9 (the extent of which is shown notionally in Fig. 1). The system, described fully in Ref. 43, is based on the $5d[4]_{7/2}-6p[3]_{5/2}$ (834.72 nm as measured in air) transition for singly charged xenon (Xe II), which fluoresces at 541.91 nm, and the $6s^2[1/2]_1^0-6p^2[3/2]_2$ (834.68 nm) transition for neutral xenon (Xe I), which fluoresces at 473.41 nm. The region of interrogation for the ion (Xe II) velocity distributions extended from $z/L_{ch} = -0.5$ to 1.3, where L_{ch} denotes the channel length from anode to exit plane. In this convention, $z = 0$ corresponds to the exit plane, and positive values are downstream of the exit plane. The spatial resolution was 1 mm near the exit plane and gradually increased to 10 mm downstream. For the neutral population (Xe I), we acquired data from $z/L_{ch} = -0.9$ to -0.3 with a constant

spatial resolution of 2.5 mm and a typical velocity resolution of 30 m/s. The spatial extent was limited to upstream of the exit plane in this case because the chosen Xe I transition fluorescence is overwhelmed by noise from Xe II emission in the downstream region.

The procedure for TA LIF measurements is, in brief, as follows: detune the laser beam to reach the desired corresponding Doppler-shifted velocity; record the laser wavelength and intensity; average the measured transduced fluorescence signal for a period ~ 1 s; and repeat for a range of velocities to reconstruct the VDF. For TR measurements, following Ref. 44, we employed a phase-sensitive detection approach involving a “boxcar averaging” system that uses a sample-and-hold circuit (SHC) referenced to variations in the thruster discharge current to filter the fluorescence signal and thereby measure VDFs phase by phase. Here, the trough in the discharge current signal is used to trigger the SHC, which samples and outputs the fluorescence signal according to a programmable delay and gate width. We evenly sampled seven phases from 0 to $65 \mu\text{s}$ with a chosen gate width of $10 \mu\text{s}$. This timing dictated a Nyquist frequency of 50 kHz, which was sufficient to resolve the breathing frequency in the present experiment. Traces were taken sequentially for a range of delays until an entire breathing cycle was characterized. We report time-resolved measurements in terms of phase delay with respect to the discharge current in this work because we acquired data over multiple experimental campaigns during which the breathing frequency varied slightly.

In order to facilitate the phase-sensitive detection technique, we operated the thruster at a condition (specified in Sec. II) where the oscillations associated with the breathing mode were naturally strong and coherent. Specifically, we selected an operating point where discharge current oscillations were $>100\%$ the mean value, and the width of the spectral peak Δf_b associated with these oscillations was relatively small, $\Delta f_b \ll f_b$. Figure 2 shows an example of

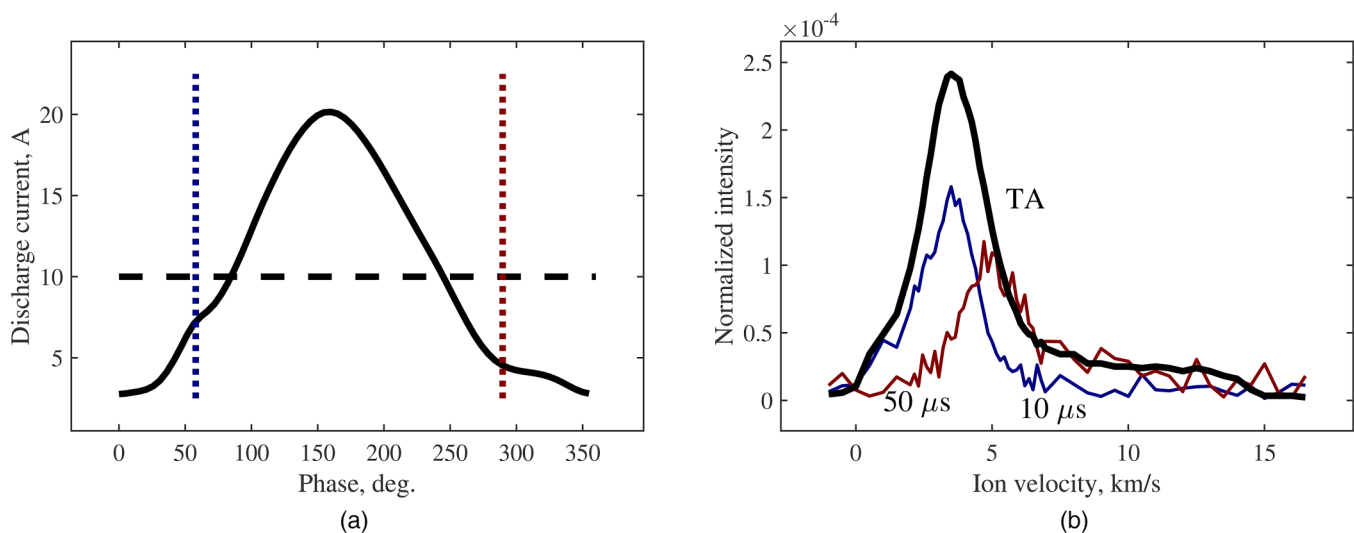


FIG. 2. The discharge current signal plotted as a function of phase (a), with two sample time-resolved VDFs measured at $z/L = -0.03$ (at phases indicated with vertical lines) shown in (b). These lines correspond to $10 \mu\text{s}$ (blue) and $50 \mu\text{s}$ (red) after the minimum in discharge current. The time-averaged (TA) VDF is shown for comparison (black).

two time-resolved VDFs measured at this operating condition, one near a phase of 50° (blue) and another 300° (red), compared to the corresponding time-averaged measurement.

B. Ion Boltzmann implicit solution

We apply an analysis approach based on a non-Maxwellian fluid model to translate the TR LIF measurements to key local plasma properties. This method is detailed thoroughly in Refs. 24 and 43 and is based on the time-averaged approach adopted by Pérez-Luna *et al.*⁴⁵ In short, this technique involves solving a series of 1D equations for the density, n , axial electric field, E_z , and ionization frequency, f_{iz} , by taking the first three velocity moments of the Boltzmann equation for the ion population. The moments (integrals over velocity space) in these equations of the VDFs are calculated directly from the LIF measurements. The resulting equations include an implicit function of n and as such, we refer to the technique as the “ion Boltzmann implicit solution” (IBIS).²⁴ However, we note that this is not formally a kinetic method as it is based on solving the fluid equations. The key assumptions for this approach are that ions move ballistically in the axial direction (that is, the ion temperature is generally much smaller than the drift velocity) and that ionization is the dominant collisional process experienced by the ions. A brief overview of the steps involved in this method is depicted graphically in Fig. 4 at the end of this section, and they are described in the following.

- Express symbolically the first three moments of the ion Boltzmann equations as functions of the velocity moments of the ion velocity distribution function (IVDF),

$$\frac{\partial n}{\partial t} + \frac{\partial \bar{u}_i n}{\partial z} = n f_{iz}, \quad (1a)$$

$$\frac{\partial \bar{u}_i n}{\partial t} + \frac{\partial \bar{u}_i^2 n}{\partial z} - \frac{e}{m} n E_z = 0, \quad (1b)$$

$$\frac{\partial \bar{u}_i^2 n}{\partial t} + \frac{\partial \bar{u}_i^3 n}{\partial z} - 2 \frac{e}{m} n E_z \bar{u}_i = 3 \frac{e}{m} T_n n f_{iz}, \quad (1c)$$

where $\bar{u}_i^j \equiv \int u_i^j f du$ is the j th velocity moment, m is the ion mass, and T_n is the neutral gas temperature. The first equation is ion continuity, the second corresponds to conservation of ion momentum, and the third is conservation of ion energy. We have assumed here that the ions are singly charged. This assumption is driven by our LIF scheme, which specifically targets an excited state of singly charged xenon. In the subsequent analysis, we continue to neglect higher charge states as previous studies have shown the majority of ions to be singly charged in the H9, yielding a charge utilization efficiency exceeding 94%.⁴⁶

- Convert the fluid equations to simple ordinary differential equations

Equation (1) can be written as a simplified system of ordinary differential equations with the addition of two assumptions. First, we assume that the highest-order moment we consider is approximately Maxwellian to simplify the ion energy

conservation equation; that is, $\bar{u}_i^3 \approx 3\bar{u}_i \bar{u}_i^2 - 2\bar{u}_i^3$. Physically, this assumption requires that the discrepancy between the actual IVDF and a Maxwellian approximation contributes negligibly to the uncertainty of \bar{u}_i^3 . In this study, we found that this discrepancy—quantified by the difference between the measured third velocity moment and that yielded by this approximation—was on average over 60 times smaller than the bulk uncertainty in the calculated moments. We thus conclude that $\bar{u}_i \bar{u}_i^2 - 2\bar{u}_i^3$ is a justifiable simplification.

Second, time dependence can be decoupled from the ion continuity equation—thus simplifying the solution of the system—if we assume that the ionization frequency is much faster than characteristic temporal changes in ion density τ , such that $f_{iz} \gg \tau^{-1}$, where $\tau \sim n^{-1} \partial n / \partial t$. This further permits the inequality $n f_{iz} \gg \partial n / \partial t$, which can be used to simplify Eq. (1a). To justify this assumption, we express the inequality as $\xi \gg f_b / n_n$ where we denote the ionization rate coefficient $\xi \equiv f_{iz} / n_n$ and we approximate the breathing frequency $f_b \approx n / (\partial n / \partial t) \sim 10$ kHz. As $n_n \sim 10^{19} \text{ m}^{-3}$ in the near-field (where fluctuation strength is anticipated to be largest), we can solve the above inequality using tabulated ionization rate coefficients⁴⁷ to find the inequality is satisfied provided $T_e \gg 2.9$ eV. This is a reasonable assumption throughout the measurement domain. We note here that this assumption about relative time scales does not exclude the possibility that other quantities similarly vary much slower than the ionization frequency. However, such further limits are not invoked because they yield no practical simplifications of Eq. (1).

A final assumption is that $T_n f_{iz} \ll E_z \bar{u}_i$. Physically, this implies that the power spent on ionizing the neutral gas is much smaller than the power spent accelerating the ions. This can be justified by considering the ionization cost of the H9, which we anticipate to be <100 eV/ion based on the performance of the H6MS, a similar magnetically shielded thruster.⁴⁸ Compared to the discharge voltage, this indicates that a majority of the discharge power is spent on acceleration.

Subject to these assumptions, we now can re-write Eqs. (1a) and (1c) in terms of the quantities of interest and the first and second velocity moments and their derivatives,

$$\frac{\partial \bar{u}_i}{\partial z} + f_n = f_{iz}, \quad (2a)$$

$$\begin{aligned} \frac{\partial \bar{u}_i^2}{\partial t} + (3\bar{u}_i^2 - 2\bar{u}_i^2) f_n + 3\bar{u}_i \frac{\partial \bar{u}_i^2}{\partial z} + 3(\bar{u}_i^2 - 2\bar{u}_i^2) \frac{\partial \bar{u}_i}{\partial z} \\ = 2 \frac{e}{m} E_z \bar{u}_i. \end{aligned} \quad (2b)$$

Note here that we have introduced the definition of an ion density gradient frequency $f_n \equiv \bar{u}_i^{-1} \partial \ln n / \partial z$ for which we can solve explicitly, instead of n .

- Solve the simplified equations explicitly for ionization frequency, electric field, and ion density gradient frequency.

Armed with the simplified equations from the previous step, we now write expressions explicitly for the three key unknowns, in which we define the total spatial derivative

$$D/Dz \equiv \partial/\partial z + \bar{u}_i^{-1} \partial/\partial t,$$

$$f_{iz} = \frac{-\bar{u}_i \frac{dD}{dz} + N + T}{D}, \tag{3a}$$

$$f_n = \frac{D\bar{u}_i}{Dz} - f_{iz}, \tag{3b}$$

$$E_z = \frac{m_i}{e} \left(\frac{\partial \bar{u}_i}{\partial t} + \frac{\partial \bar{u}_i^2}{\partial z} - \frac{\bar{u}_i^2}{\bar{u}_i} f_n \right), \tag{3c}$$

where

$$N \equiv \frac{d\bar{u}_i}{dz} (2\bar{u}_i \bar{u}_i^2 + D),$$

$$D \equiv 2\bar{u}_i \bar{u}_i^2 - \bar{u}_i^3,$$

$$T \equiv \bar{u}_i \frac{\partial \bar{u}_i^2}{\partial t} - 2\bar{u}_i^2 \frac{\partial \bar{u}_i}{\partial t}.$$

- Evaluate Eq. (3) using the velocity moments measured with LIF. We have now expressed f_{iz} , f_n , and E_z explicitly in terms of ion velocity moments and their derivatives. The velocity moments are calculated from measured IVDFs with trapezoidal numerical integration, and the derivatives computed numerically using a second-order finite difference scheme. With these values, we then can sequentially solve Eqs. (3a), (3b), and (3c).
- Solve for n by integrating along ion trajectories.

Now that f_n has been calculated, n can be found explicitly in a Lagrangian sense; that is, along ion trajectories f_n is strictly a function of $D\bar{u}_i/Dz$ and f_{iz} . As a result, we may use Eq. (3b) to solve for the ion density along ion trajectories,

$$n(z) = n(z_b) \exp \left[\int_z^{z_b} \bar{u}_i f_n dz \right]. \tag{4}$$

Here, z_b is a boundary location where the ion density is known. To acquire the boundary value $n(z_b)$, we used a small (~ 3 -mm diameter) planar Faraday probe biased to -40 V with a foil guard electrode to measure the ion current density j_i in the near-plume. The probe was injected with a high-speed motion stage to a measurement point coincident with our most downstream LIF point (far downstream of the acceleration zone). Knowing \bar{u}_i from LIF and j_i from the Faraday probe, we then used the relation $n = j_i/e\bar{u}_i$ to determine ion density assuming all ions have a single fundamental charge e . Figure 3 shows the notional layout for this configuration.

- Using f_{iz} , determine u_n and n_n by finding shooting solutions of the first two moments of the neutral Boltzmann equation. For this step, we consider the quasi-1D fluid continuity and momentum conservation equations for neutrals

$$\frac{Du_n}{Dt} = \frac{nf_{iz}}{n_n}, \tag{5a}$$

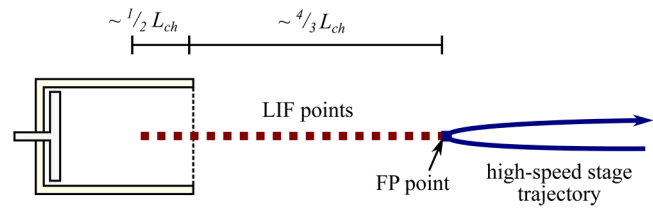


FIG. 3. Diagram of the measurement configuration, where LIF points are taken inside the channel and in the near-plume, and a single Faraday probe point is taken coincident with the most downstream LIF measurement.

$$\frac{Dn_n}{Dt} = -2nf_{iz} - \frac{u_n n_n}{A_n} \frac{dA_n}{dz}, \tag{5b}$$

where we have denoted the total derivative here as $D/Dt \equiv \partial/\partial t + u_n \partial/\partial z$ and A_n is the cross-sectional area of the neutral plume. We assume that this area is identical to the channel cross-sectional area for $z < 0$, and $A_n \approx 2\pi r(2z + w)$ for $z > 0$. This formulation for the area is based on the assumption that the neutral plume expands semi-hemispherically outside the thruster channel. We solve Eq. (5) by first inserting our temporally and spatially resolved measurements for ionization frequency from IBIS (Step 4). This thus renders the two equations in terms of two unknowns, the neutral density and velocity. We then measure boundary conditions for n_n and u_n and integrate the equations numerically from these points. The result yields values for neutral density and velocity as a function of time at all locations in the spatial domain.

For the boundary condition of the neutral velocity, we used the most downstream time-resolved measurement from the Xe I LIF, located at $z/L_{ch} = -0.3$. For the boundary condition of the neutral density, we invoked the relationship $n_n \equiv f_{iz}/\xi(T_e)$, which we evaluated with local plasma measurements at the most downstream point of the Xe II LIF. The ionization rate coefficient $\xi(T_e)$ was found from tabulated values as a function of electron temperature, which was measured directly at the boundary point in a time-resolved fashion. This was done with a high-speed cylindrical Langmuir probe injected with the same configuration as the Faraday probe described in Step 5 (Fig. 3). In practice, we found that the time-averaged value of f_{iz} was very small compared to its uncertainty at the boundary location, so we sought a different estimate of the time-averaged f_{iz} to supplement the IBIS results. Specifically, we found that the time-average of T_e yielded by the Langmuir probe; we estimated a time-averaged n_n at the boundary by invoking ion and neutral particle conservation; and then we computed a time-averaged f_{iz} via the definition $f_{iz} \equiv n_n \xi(T_e)$. To find n_n as part of this process, we assumed the flux of hot neutrals from the anode must be balanced by the flux of un-ionized neutrals emerging from the channel and the flux of ions exiting the thruster.

- Calculate electron temperature from the neutral and ion properties.

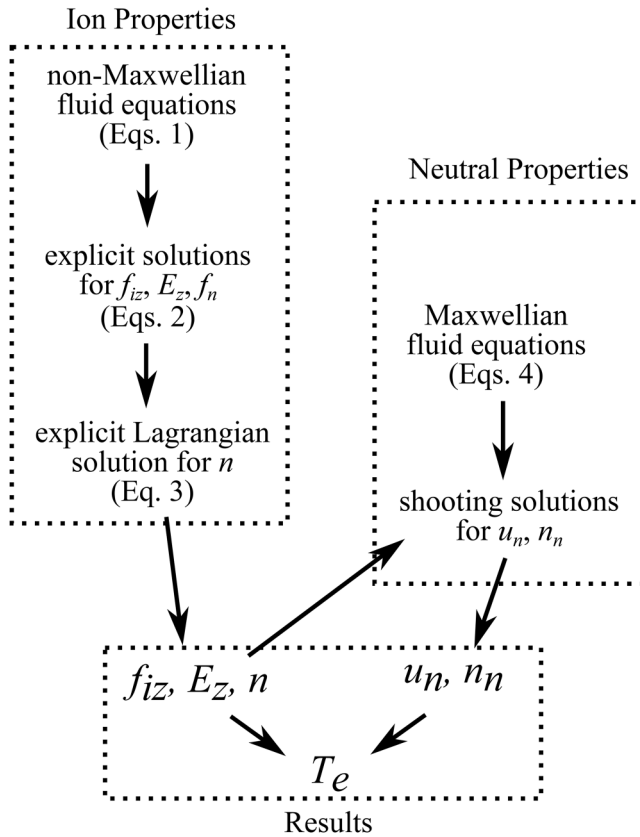


FIG. 4. Flow chart illustrating the execution of IBIS analysis for both ions and neutrals.

As a final step, we combine the measured values of neutral density and ionization frequency to infer the local distribution of electron temperature using the relationship $\xi(T_e) \equiv f_{iz}/n_n$. In this case, we used the values of f_{iz} determined from IBIS (Step 4) and n_n estimated with Eq. (5) (Step 6) to calculate f_{iz}/n_n . We then used tabulated values of $\xi(T_e)$ to solve for temperature.

In summary, we have shown that non-invasive LIF and minimally invasive electrostatic probe measurements can be combined with a model based on taking moments of the measured ion kinetic distribution to estimate a variety of time-resolved ion properties. The application of neutral fluid equations can then yield neutral properties. Finally, a combination of this ion and neutral information can shed light on key electron properties like T_e . Figure 4 provides a final summary of the entire IBIS process, with specific reference to the relevant equations.

IV. RESULTS

We now present the results of this experimental campaign, starting with the time-averaged information yielded by the IBIS

method described in Sec. III B and then proceeding to the time-resolved results. We end this section by summarizing key observations for the measured plasma fluctuations.

A. Time-averaged results

We first show in Fig. 5 results illustrating the background plasma properties against which the oscillations propagate, calculated as the temporal mean of our inferred time-resolved data. That is, each quantity is determined as a function of time and then averaged over several breathing mode cycles to produce a mean value along the channel centerline. Per our discussion of methodology in Sec. III, only the ion velocity and the (upstream) neutral velocity were directly measured with LIF; all other parameters (including the neutral velocity downstream of $z = -0.3$) are measured with the IBIS technique.

Figure 5(a) shows the trends in both time-averaged neutral and ion velocities. We have estimated uncertainty in these results by first performing a least-squares fit of at most three Gaussians to the measured VDF. The difference between the raw velocity moment calculated from the data and that inferred by the least-squares fit is taken as a measure of uncertainty. The trends exhibited by both velocity profiles are typical for Hall thrusters. The ion velocity stagnates approximately halfway through the channel, becoming increasingly negative into the anode sheath and positive through the acceleration region. The velocity downstream ultimately reaches a value of nearly 19.5 km/s. The neutral velocity in the region immediately downstream of the anode ($z/L_{ch} = -1$ to -0.3) is relatively constant, with a mean drift of 190 m/s. This is comparable to the anticipated thermal speed of ~ 100 m/s that we would expect from choked flow through the hot (400–500 °C) anode. This measured neutral speed similarly is consistent with the values observed in previous Xe I LIF studies.^{49,50} We note that there is a slight acceleration of the neutral population through the channel. This effect also has been measured in other studies and attributed to wall accommodation, selective ionization, and charge-exchange.⁵⁰

Figure 5(b) shows plots of the neutral and ion density as a function of position. The uncertainty here, as in Figs. 5(c) and 5(d), is calculated by repeatedly producing normal samples of the velocity moments based on their calculated variance and then performing the IBIS analysis on these sample sets. The variance of the resulting sets of f_{iz} , E_z , and f_n (and thus n) values is used as a measure of their random error. With these uncertainties in mind, the ion density decreases monotonically with the position in the measured domain. Physically, this profile is dictated by a balance of ionization and acceleration. The former effect drives an increase in the density while the latter, by continuity, leads to a decrease. Our result indicates that we have measured sufficiently downstream that the acceleration effect dominates, leading to the monotonically decreasing profile. The neutral density profile, like that for ions, monotonically decreases with the position. This decrease can be attributed to a number of phenomena including wall accommodation, depletion by ionization, and expansion of the neutral plume into vacuum.

Figures 5(c) and 5(d) show plots along the channel centerline of the time-averaged ionization frequency, electric field, electron

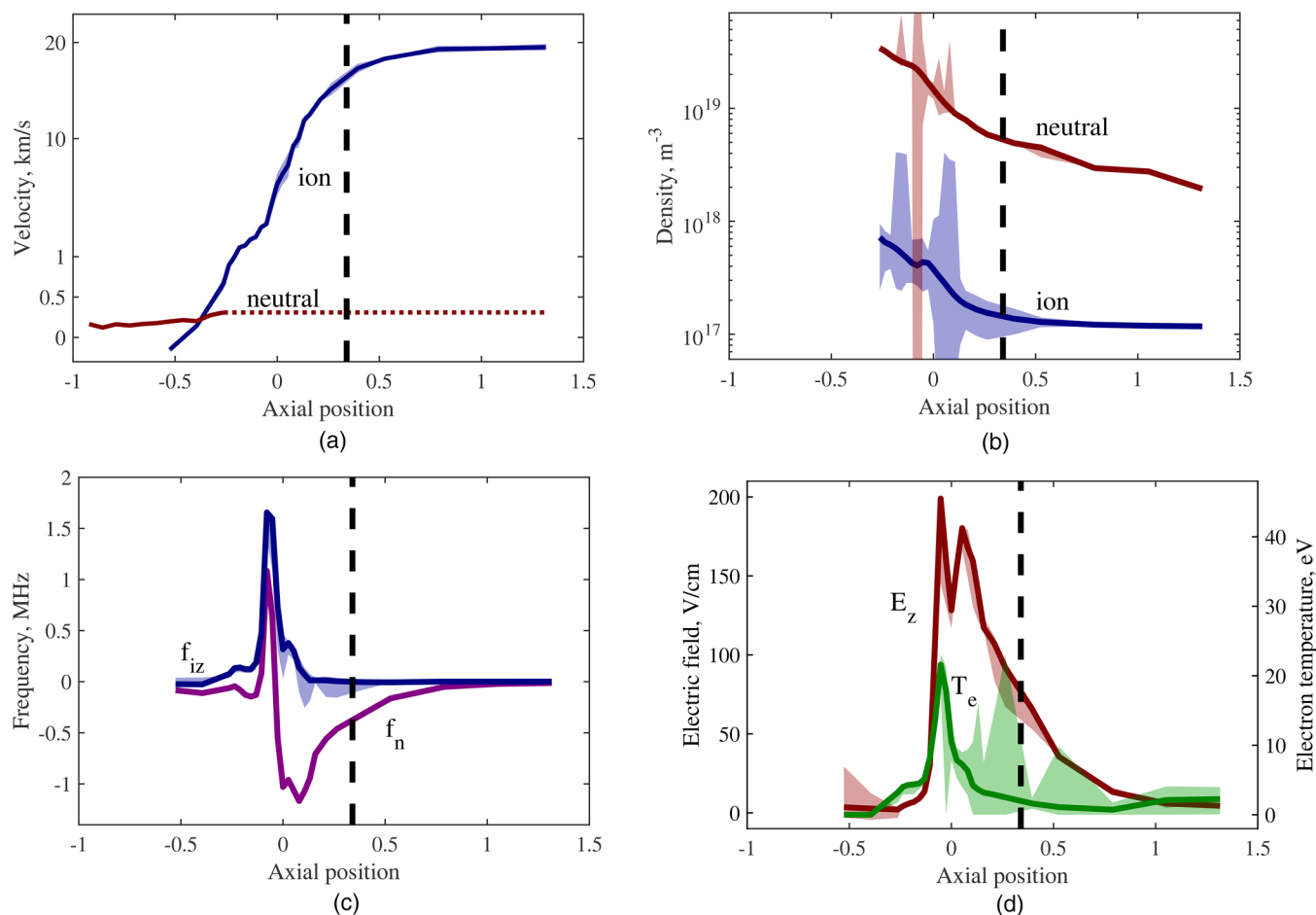


FIG. 5. Time-averaged plasma properties as a function of the axial position including the mean ion and neutral velocities (a); ion and neutral densities (b); ionization frequency (c); and electric field strength and electron temperature (d). Uncertainty is indicated with shaded regions. The exit plane of the thruster is coincident with the axial position of zero, and all lengths are normalized to the channel length. The dashed vertical line denotes the location of peak magnetic field strength. Note that in (a), both the directly measured (solid) and IBIS-calculated (dashed) u_n values are shown. A power law ordinate scale is used to accentuate the neutral velocity profile.

temperature, and ion density gradient frequency. We note that since f_{iz} cannot be negative, any measurements inferred to be below zero due to uncertainty are limited to zero. The justification for correcting these negative values as a numerical artifact is provided in [Appendix A](#).

There are several notable trends in these measured values that are consistent with the nominal operation of the Hall thruster. First, the electric field is nearly coincident with the location of the peak magnetic field (shown as a dashed black line). This is because the cross-field motion of the electrons is most inhibited in the region of the strongest magnetic confinement. Second, the electron temperature profile mirrors the electric field profile. This can be attributed to the dominance of Ohmic heating in the plasma. Third, the peak in ionization frequency is located upstream of the peak in the electric field. This stems from the fact that ionization depends both on temperature and neutral density. As the neutral

density decreases monotonically while the electron temperature exhibits a peak, we expect ionization frequency should exhibit a maximum upstream of the maxima in electron temperature and electric field. The spatial difference in peak electric field and ionization frequency illustrates the oft-cited separation of the so-called ionization and acceleration zones in these devices.

B. Time-resolved results

1. Discharge current

[Figure 6](#) shows two cycles of the breathing mode in a typical discharge current waveform and the corresponding power spectra for the oscillatory operating condition we examined in this work. As the spectrum shows, the breathing mode is especially coherent at this operating condition, facilitating the phase-averaged time-resolved LIF technique we employed in this study. As described in

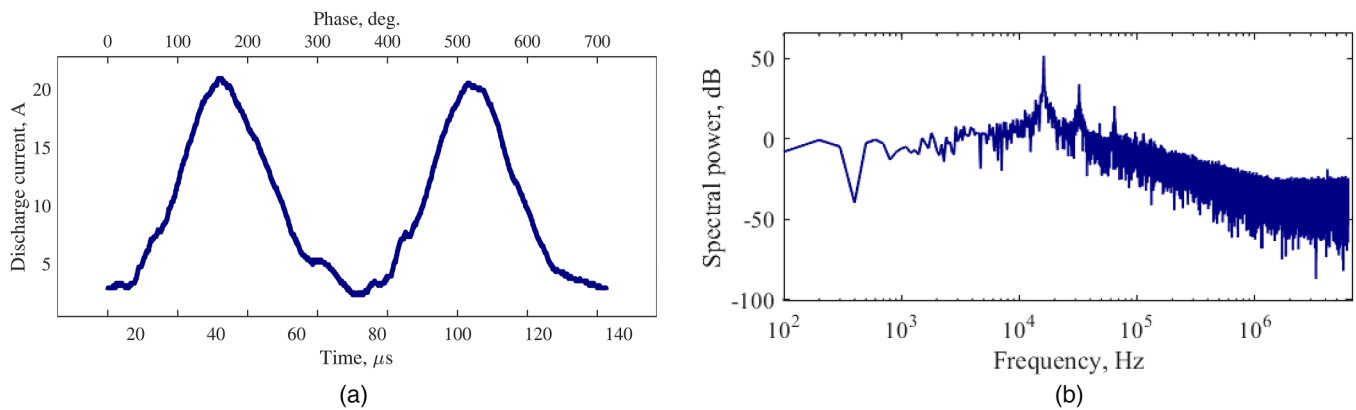


FIG. 6. (a) Representative time dependence of discharge current as a function of time at 300 V and 3 kW. (b) Power spectrum of discharge current oscillations.

Sec. III A, we hereafter show time-resolved results as a function of the phase of the breathing mode since all measurements are phase-averaged.

2. Raw plasma properties

All quantities shown in Sec. IV A were also measured in a time-resolved way as a function of the phase of the breathing mode. To visualize these fluctuations, we show in Fig. 7 the variations in electron temperature and ion and neutral densities and velocities as a function of phase and axial position. In each case, we have normalized the global maximum of each quantity but otherwise the shape of the maps is unaltered. Several faint trends can be observed in these plots. In particular, u_i , n , and T_e appear to fluctuate temporally but are dispersionless (i.e., do not convect) while n_n does show dispersion, and u_n does not seem to fluctuate with any coherence. The oscillations in n and T_e are particularly strong, varying as much as 20%/μs at a given axial position. These intense temperature and density fluctuations suggest the processes governing electron heating are varying over a breathing cycle. This is consistent with observations from previous experimental studies.^{24,32} The link between electron heating and the breathing mode also has previously been remarked upon in a number of numerical studies (cf. Refs. 18, 27, and 51). Figures 7(c) and 7(e) show that the acceleration region, as represented by the location where ion velocity exhibits a step-like increase, appears to move downstream at the peak in I_d and upstream at the trough. Similar types of movement in the acceleration zone have been observed in previous experimental studies based on LIF measurements.^{24,44,52–56}

3. Normalized plasma properties

While the plots in Fig. 7 illustrate trends in the oscillations of various quantities, the large scale variations can obscure information on the relative propagation of these fluctuations. In order to better highlight these trends, we have rescaled them in Fig. 8. Figures 8(a) and 8(b) are plotted with the magnitudes rescaled between 0 and 1 at each spatial location, e.g., $\tilde{n}(z, t) = [n(z, t) - n_{\min}(z)]/[n_{\max}(z) - n_{\min}(z)]$, where n_{\min} and

n_{\max} are the density extrema as a function of axial position. The remainder of the quantities are rescaled at each phase, e.g., $\tilde{u}_i(z, t) = [u_i(z, t) - u_{i,\min}(t)]/[u_{i,\max}(t) - u_{i,\min}(t)]$, where $u_{i,\min}$ and $u_{i,\max}$ are the velocity extrema as a function of time. These separate scaling schemes are used to emphasize the types of waves that are dominant for each quantity: rescaling at each axial location helps illustrate relatively slow waves, while rescaling at each phase illustrates fast (dispersionless) waves. This choice of scale is for plotting only and does not influence any later analysis.

Besides a slight deviation near $z/L_{ch} = 0.1$, ion density fluctuations—tracked notionally with the red dotted trend line—do, in fact, propagate, and they do so at speeds close to the ion drift velocity. This contrasts with the raw Fig. 7(a), in which this trend was unclear. The phase offset across the axial domain is roughly $\sim 50^\circ$, yielding an average phase speed of ~ 10 km/s. This observation appears consistent with previous experimental studies of the breathing mode oscillation showing that density perturbations associated with this mode propagate downstream near the ion drift velocity.^{32,33} Figure 8(b) shows the fluctuation in neutral density, which appears to drift near the mean neutral gas velocity in this region, roughly 300 m/s, as shown with the notional trend lines. Farther downstream, the broad spatial resolution leads to aliasing (apparent changes in wavelength due to undersampling) of these n_n waves, although upstream of $z/L_{ch} \approx 0.3$, the trend is unambiguous. Ultimately, this result suggests that the neutral density fluctuations exhibit a traveling wave correlated with the breathing mode that propagates downstream through the ionization zone. The fact that the neutral population should exhibit a traveling wave has been proposed previously as the result of one-dimensional quasi-steady numerical work by Barral and Peradzyński,²⁸ though to our knowledge, this is the first experimental evidence of this effect.

Figures 8(c)–8(e) show maps of relative fluctuations in u_i , u_n , and T_e . As in Figs. 7(c) and 7(e), no spatial trends in the u_i and u_n fluctuations are apparent, and again u_n does not seem to oscillate coherently at all. Similarly, electron temperature fluctuations appear to be dispersionless, although there is certainly a slight

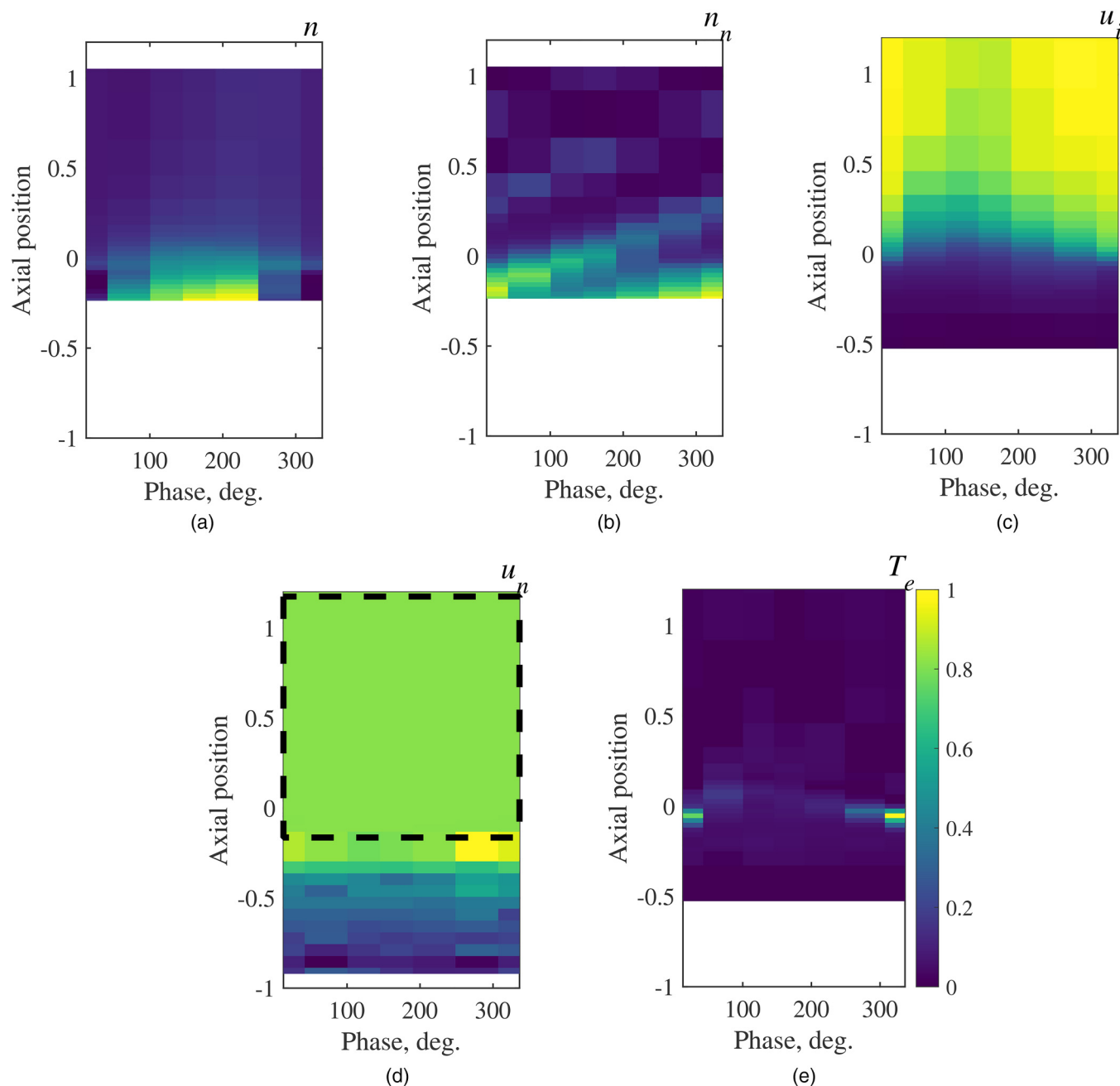


FIG. 7. Fluctuation strength for ion and neutral density [(a) and (b)]; ion and neutral velocity (c) and (d); and electron temperature (e). Each quantity is normalized relative to its global maximum exhibited during oscillation: $n = 1.2 \times 10^{18} \text{ m}^{-3}$, $n_n = 4.4 \times 10^{19} \text{ m}^{-3}$, $u_i = 20.8 \text{ km/s}$, $u_n = 367 \text{ m/s}$, and $T_e = 86 \text{ eV}$. The portion of u_n that was calculated from neutral fluid equations is enclosed in the dashed box.

displacement of the peak in T_e throughout a breathing cycle. Indeed, all electron-related quantities we measured fluctuate in this manner. This relative lack of propagation may in part be attributed to the fact that the electron transit times are much faster than those

of the ions and neutrals. As a result, the changes in these quantities appear to happen almost instantaneously on the timescale of the breathing oscillations and thus the modes are dispersionless within the limitations of our diagnostic technique.

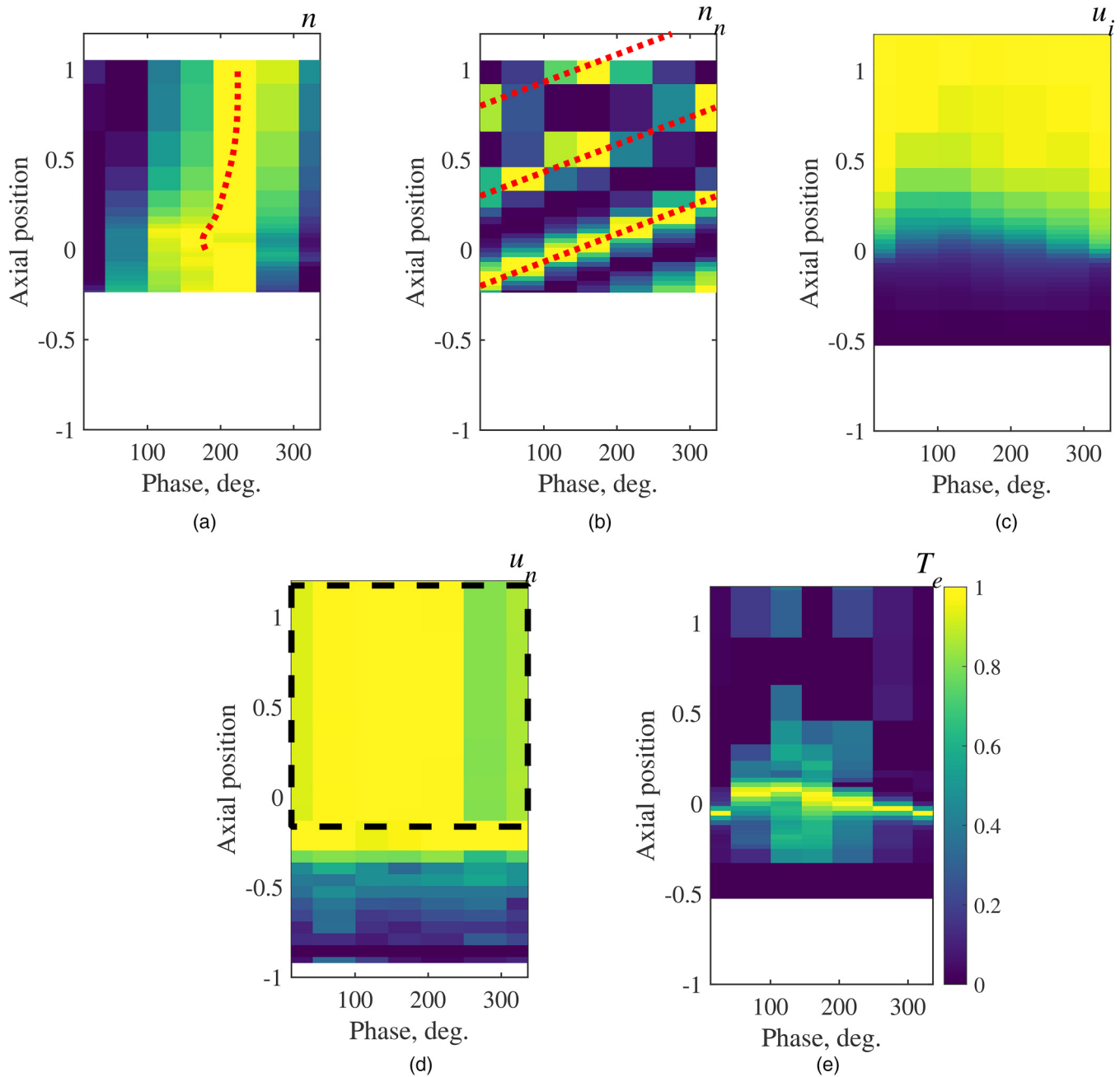


FIG. 8. The rescaled fluctuation strength for ion and neutral density [(a) and (b)]; ion and neutral velocity [(c) and (d)]; and electron temperature (e). The portion of u_n that was calculated from neutral fluid equations is enclosed in the dashed box.

4. Phase velocities of observed waves

While Fig. 8 shows qualitative trends in the densities, we can perform a frequency-domain analysis to provide additional quantitative insight into both the phase velocity and amplitude variation

of the observed waves. We assume that all fluctuations can be described sinusoidally in time at any axial location such that, for example, $\tilde{n}(z, t) = \hat{n}(z) e^{-i\omega(z)t + \theta(z)}$. In doing this, we require that the oscillations are sufficiently coherent (according to our criteria in Sec. III A) that this approximation is valid. Although this may

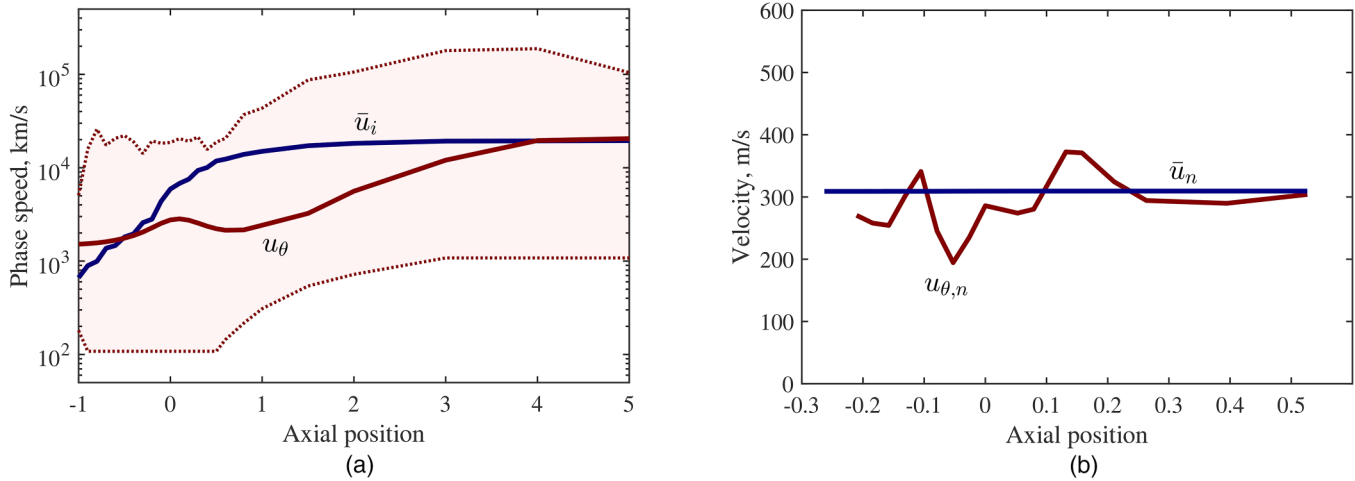


FIG. 9. Measured phase speed of ion (a) and neutral (b) density fluctuations compared to the mean velocity as a function of axial position. Shaded regions indicate estimated uncertainty in the measured phase speed.

not be true for the large amplitude of n fluctuations, we find later that the uncertainty of these measurements is large enough that this issue can be overlooked *a posteriori*. Using the component of the Fourier transform at the measured breathing frequency, any fluctuating quantity can be described as a phasor quantity, e.g., $\mathcal{F}[\hat{n}](z) = \hat{n}(z)\angle\theta(z)$. In this way, the Fourier transform can be used to determine the wave amplitude \hat{n} and phase θ as a function of axial location. Once the phase is known, the phase velocity u_θ can be calculated from the definition $\omega \equiv u_\theta\partial\theta/\partial z$.

With this approach in mind, we show the results of the frequency space analysis in Figs. 9 and 10. The former shows the axial

evolution of the spline-smoothed phase speed of ion and neutral density fluctuations, u_θ and $u_{\theta,n}$ respectively, with the drift speed of each species included for comparison. The neutral density waves propagate quite close to the drift speed over the whole domain. The uncertainty in $u_{\theta,n}$ is not plotted as it is negligible here. On the other hand, the phase speed of the ion density waves matches much less definitively. There is reasonable agreement between the two upstream and improved agreement far downstream but a significant discrepancy between these regions.

The sizable uncertainty of the ion phase velocity values must be addressed. The upper limit is computed by bootstrapping:⁵⁷ the error in phase is estimated as $\omega\Delta t$ for a temporal resolution of the time-resolved LIF system Δt , the measured phase profile is resampled using this uncertainty, and finally the sample phase velocity is computed. Repeating this many times, the uncertainty in the phase velocity can be found as an upper percentile of the resampled velocities. The lower limit is related to the phase resolution of the diagnostic for axial points spaced by Δz : waves propagating slower than $\Delta z/\Delta t$ are indistinguishable from stationary and thus cannot be detected by our time-resolved LIF system. Therefore, any observed waves must be propagating faster than that limit. The large scale of the total uncertainty is not unexpected as not only is there ambiguity in the determination of phase (elaborated in Appendix B) but also the possibility of aliasing permits spurious phase velocity measurements. In total, the diagnostic technique used in this study is not fast enough to accurately resolve the ion phase speed. For this reason, we do not attempt to draw any quantitative conclusions about u_θ but instead interpret it qualitatively. In this case, we find that our ion wave measurements are qualitatively consistent with waves propagating at the ion drift speed.

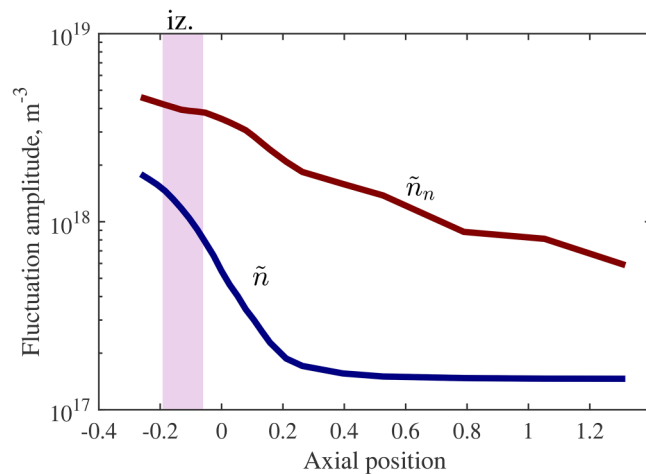


FIG. 10. The fluctuation strength for ion and neutral density as a function of axial position. The range of locations of peak ionization frequency is shown as a shaded region.

5. Spatial variation in amplitudes of observed waves

Figure 10 shows the measured amplitude profiles of \tilde{n} and \tilde{n}_n , linearly smoothed with a moving average $L_{ch}/8$ wide. The

ionization region can be identified as the range of locations of peak f_{iz} over a breathing cycle, in which case the ionization zone is centered on average near $z/L_{ch} = -0.13$ [corroborated by Fig. 5(c)]. It is evident that the fluctuation amplitude is not only nonzero upstream of the ionization zone but consistently decreases throughout the measurement domain. This result seems to indicate that the mode decays over the entire experimental domain. Further, this finding shows experimentally that the plasma properties of the discharge upstream of the ionization zone fluctuate with the breathing mode frequency. This suggests that the near-anode plasma conditions may be related to the oscillation. We return to this point in Secs. V B 1 and V B 2.

6. Summary of key findings

In summary, the goal of this experimental investigation was to characterize the oscillation of plasma properties inside the thruster channel on the time-scale of the breathing mode. Applying the IBIS technique to this task has led to the following notable observations:

- Neutral density fluctuations propagate coherently with a phase velocity approximately equal to the neutral drift velocity.
- Ion density fluctuations propagate coherently with a phase velocity on the order of the ion drift velocity.
- Electron properties are dispersionless (no detectable spatial propagation) on the time scale of the breathing mode.
- Neutral and ion oscillations spatially decay in the ionization and acceleration regions.

We discuss the implications of these new experimentally informed physical insights in the next section.

V. DISCUSSION

Armed with the measurements from Sec. IV, we now can discuss the type of waves we observed, the evolution of their amplitude throughout the channel, and possible processes governing the breathing mode. To start, we separately examine the propagation of ion and neutral density fluctuations to identify a dispersion relation appropriate for describing the measured waves present in the channel. Next, we interpret the amplitude trends in Fig. 10 in the context of these dispersion relations. Finally, we use these findings to synthesize hypotheses for the process of controlling the breathing mode.

A. Theoretical dispersion

The first aspect of the measured fluctuations that we investigate is the dispersion of the waves. In particular, we are motivated by the observation that there appear to be two disparate waves, one associated with the neutrals and one associated with the ions that move downstream from the ionization region. While a limited set of previous numerical studies have commented on the possibility of the oscillations associated with the breathing mode—particularly those in neutral gas properties—exhibiting a traveling or convecting component (cf. Ref. 18), the theory underlying these predictions does not easily lend itself to a comparison to our experimental data. With this in mind, we re-derive here a simplified theoretical

justification for how it is possible that two waves with disparate length scales and propagation speeds might exist in the discharge.

For this discussion, we only consider the dispersion where ionization is negligible, i.e., in the region downstream of the main ionization zone, i.e., $z/L > 0.2$ in Fig. 5. The choice to focus on this location is dictated largely by expedience as it significantly simplifies the analysis and presents an unambiguous result for both ion and neutral modes. We explore in subsequent sections the extensibility of this dispersion to conditions where this assumption is relaxed. With this in mind, neglecting ionization, the continuity equations for both species are given by

$$\frac{\partial n}{\partial t} + \frac{\partial[nu_i]}{\partial z} = 0, \tag{6a}$$

$$\frac{\partial n_n}{\partial t} + \frac{\partial[n_n u_n]}{\partial z} = 0. \tag{6b}$$

By eliminating the source terms, we have effectively decoupled the two continuity equations. This lends itself to a tractable solution in the wave dispersion analysis. In particular, we perturb each quantity to first order, yielding

$$\frac{\partial \tilde{n}}{\partial t} + \frac{\partial \left[\bar{n} \tilde{u}_i \left(\frac{\tilde{u}_i}{\bar{u}_i} + \frac{\tilde{n}}{\bar{n}} \right) \right]}{\partial z} = 0, \tag{7a}$$

$$\frac{\partial \tilde{n}_n}{\partial t} + \frac{\partial \left[\bar{n}_n \tilde{u}_n \left(\frac{\tilde{u}_n}{\bar{u}_n} + \frac{\tilde{n}_n}{\bar{n}_n} \right) \right]}{\partial z} = 0, \tag{7b}$$

where we have introduced the notation \tilde{n} to denote the fluctuating quantities and \bar{n} to denote the time-averaged background values. Based on our measurements, we argue in the downstream region that the relative fluctuations in ion and neutral velocities are smaller than the respective fluctuations in density: $|\tilde{u}_i/\bar{u}_i| \ll |\tilde{n}_i/\bar{n}_i|$ and $|\tilde{u}_n/\bar{u}_n| \ll |\tilde{n}_n/\bar{n}_n|$. We thus find

$$\frac{\partial \tilde{n}}{\partial t} + \frac{\partial \tilde{n} \bar{u}_i}{\partial z} = 0, \tag{8a}$$

$$\frac{\partial \tilde{n}_n}{\partial t} + \frac{\partial \tilde{n}_n \bar{u}_n}{\partial z} = 0. \tag{8b}$$

Our experimental measurements from Sec. IV have shown that we can represent these fluctuating quantities as sinusoids. Specifically, these are given locally in complex space by

$$\tilde{n} = \hat{n}(z) e^{i(\theta_i(z) - \omega t)}, \tag{9a}$$

$$\tilde{n}_n = \hat{n}_n(z) e^{i(\theta_n(z) - \omega t)}, \tag{9b}$$

where we have introduced real amplitudes denoted by \hat{n} and \hat{n}_n which are a function of axial position, and we have assumed all fluctuating parameters oscillate at a common breathing frequency ω . The relative phases of these fluctuations with respect to the discharge current are given by θ , where we note that the phases for

the neutral and ion density fluctuations depend explicitly on position. Substituting these results into Eq. (9) yields

$$-i\omega\hat{n} + i\frac{\partial\theta_i}{\partial z}\hat{n}\bar{u}_i + \frac{\partial\hat{n}}{\partial z}\bar{u}_i + \frac{\partial\bar{u}_i}{\partial z}\hat{n} = 0, \quad (10a)$$

$$-i\omega\hat{n}_n + i\frac{\partial\theta_n}{\partial z}\hat{n}_n\bar{u}_n + \frac{\partial\hat{n}_n}{\partial z}\bar{u}_n + \frac{\partial\bar{u}_n}{\partial z}\hat{n}_n = 0. \quad (10b)$$

If we define the fluctuation phases θ_i and θ_n such that the wave amplitudes are real quantities, the above set of complex equations yields four real-valued relations,

$$\mathbf{0} = \begin{bmatrix} -\omega + u_0 \frac{\partial\theta_i}{\partial z} & 0 \\ \frac{\partial\bar{u}_i}{\partial z} & \bar{u}_i \end{bmatrix} \cdot \begin{bmatrix} \hat{n} \\ \frac{\partial\hat{n}}{\partial z} \end{bmatrix}, \quad (11a)$$

$$\mathbf{0} = \begin{bmatrix} -\omega + \bar{u}_n \frac{\partial\theta_n}{\partial z} & 0 \\ \frac{\partial\bar{u}_n}{\partial z} & \bar{u}_n \end{bmatrix} \cdot \begin{bmatrix} \hat{n}_n \\ \frac{\partial\hat{n}_n}{\partial z} \end{bmatrix}. \quad (11b)$$

In order to ensure there are non-trivial solutions for the amplitudes of these oscillations, the determinant for each relation must be zero. We, therefore, find that for the ions and neutrals, respectively,

$$\omega = u_0 \frac{\partial\theta_i}{\partial z}, \quad (12a)$$

$$\omega = \bar{u}_n \frac{\partial\theta_n}{\partial z}. \quad (12b)$$

This result shows that strictly from continuity, both ion and neutral waves can exist, where the predicted fluctuations should move near their respective drift speeds.

We remark here that the simplified dispersion in Eq. (12) contrasts with many 0D perturbation analyses that have been performed on the breathing mode to date (cf. Refs. 4 and 19 or 58 for an overview). In these cases, a 0D model for the ionization zone is derived based on the ion and neutral continuity equation, and additional governing equations for momentum or energy are added in an attempt to identify energy sources that can promote the growth of the instability. With that said, in many of these cases—regardless of the growth rate—the analysis typically leads to the conclusion that the 0D dispersion relation (the relationship between the frequency and parameters like the length scale of the ionization zone L_{iz}) should scale as the geometric mean of the characteristic drift speeds of the ions and neutrals: $\omega \sim \sqrt{u_i \bar{u}_n} / L_{iz}$. To extend this to 1D in a simple fashion, we may assume $1/L \sim k \approx \partial\theta_n / \partial z$ or $1/L \sim k \approx \partial\theta_i / \partial z$, where k denotes wavenumber. This would yield the conclusion that for convective waves, $\omega \sim \sqrt{u_i \bar{u}_n} \partial\theta_i / \partial z$ or $\omega \sim \sqrt{u_i \bar{u}_n} \partial\theta_n / \partial z$. That is, the convecting oscillation should translate with a velocity that is the geometric mean of the two drift speeds. This has the intuitive interpretation that the ionization mode captured with a pseudo-1D model is an effective hybrid of the characteristic time scales of the two species. However, our simplified analysis has shown that, at least when

ionization is neglected, it is also a valid solution for two waves with different speeds to propagate concurrently.

As for the evolution of the amplitude of the waves, we can substitute the solutions of Eq. (12) into Eq. (11) and relate wave amplitudes \hat{n} and \hat{n}_n to steady-state quantities \bar{n} and \bar{n}_n . This yields

$$\frac{1}{\hat{n}_n} \frac{\partial\hat{n}_n}{\partial z} = -\frac{1}{\bar{u}_n} \frac{\partial\bar{u}_n}{\partial z} = \frac{1}{\bar{n}_n} \frac{\partial\bar{n}_n}{\partial z}, \quad (13a)$$

$$\frac{1}{\hat{n}} \frac{\partial\hat{n}}{\partial z} = -\frac{1}{\bar{u}_i} \frac{\partial\bar{u}_i}{\partial z} = \frac{1}{\bar{n}} \frac{\partial\bar{n}}{\partial z}, \quad (13b)$$

where we remind the reader that the hat quantities, e.g., \hat{n} , refer to the amplitude of the propagating waves while the bar quantities, e.g., \bar{n} , refer to the steady-state values. Equation (13) shows that in the absence of source terms like ionization, the fractional change in wave amplitude is predicted to decay proportionally with the change in the background density. This means that, given a consistent decrease in background density due to the acceleration of the ions and expansion of the neutral plume—effects that are captured hydrodynamically—we would expect to see a decrease in wave amplitude throughout the thruster channel. Note that this does not necessarily indicate that the wave is losing energy; rather, the wave amplitude is simply scaling with the background changes in density.

In summary, in this section, we have shown that subject to the simplifying assumptions consistent with the measured properties of the waves, it is theoretically possible for concurrent neutral and ion drift waves with different wavelengths to propagate downstream of the ionization region. This result is consistent with our experimental findings. Furthermore, when source terms are absent (negligible ionization), these predicted waves exhibit a decay in amplitude that stems from the hydrodynamic expansion of the ions and neutrals.

B. Measured dispersion

Now that we have theoretically motivated the concurrent propagation of ion and neutral waves with phase velocities commensurate with the drift speed, and we examine our experimental findings in this context. In particular, we use our experimental measurements of the background properties to evaluate the theoretical dispersion and compare these results to our measured dispersion. We note here that we first focus on a comparison to measurements where the assumptions of the theory are valid, i.e., downstream of the ionization zone, $z/L > 0.2$. However, we also comment on the potential extensibility of this simple theory to describe behavior upstream of this region.

1. Neutrals

We first remark on the measured dispersion of the neutral oscillations as shown in Fig. 8(b). Consistent with our theoretical finding in Eq. (12), these oscillations do in fact appear to propagate at the average neutral drift speed. Indeed, we see marked agreement with theory across the entire measurement domain. This is a notable result particularly in light of the fact that our theoretical dispersion was only derived for the case where ionization is

neglected. This result suggests that this dispersion is still appropriate for phenomenologically describing the wave in other parts of the domain (i.e., for $z/L < 0.2$).

While the theoretical underpinnings for why the dispersion is extensible upstream of the ionization region is not readily apparent, the observation that the neutral oscillations match the dispersion relation for neutral drift waves everywhere in the domain draws an interesting contrast with previous numerical and perturbation studies (e.g., Refs. 5 and 59). In these past works, the neutral gas was often interpreted as having a “front” with an oscillating axial position; that is, contours of constant n_n are approximately sinusoidal in z - t space. In this case, variations in the neutral gas density profile are observed to shift back and forth in bulk like a standing wave [much like the electron temperature profile in Fig. 8(e)] without an associated convection of the perturbed quantities at a finite phase speed. As we have discussed in Sec. IV, to our knowledge, only a limited number of theoretical and numerical investigations, such as by Barral and Ahedo,¹⁸ have predicted the presence of traveling neutral waves more consistent with the dispersion we report here.

As an additional observation, it is interesting to note that the neutral waves, which travel downstream at the neutral drift speed, appear to propagate from a location *upstream* of the ionization region, which is on average located around $z/L_{ch} = -0.13$. While the breathing mode is traditionally seen as an instability sustained in the ionization and acceleration zones (starting with the simulations of Fife *et al.*⁴ and continuing into recent reviews⁶⁰), the results of the present study imply that the neutral gas flow is already modulated upstream of those regions. The mechanism driving this modulation upstream remains an open question, though some recent numerical work by Smolyakov *et al.*²² has suggested that this process might be attributed to recombination from backstreaming ions. With that said, we emphasize that although we see the neutral oscillations propagate from a location upstream of the ionization zone, this does not necessarily imply that the energy source responsible for driving these modulations unstable is also localized to this upstream region. We expand upon this point in Sec. V E.

2. Ions

We next turn to an interpretation of our ion results in the context of the theory outlined in Sec. V B. Figure 9 shows a comparison of the predicted dispersion [Eq. (9)] and the measured dispersion. Unlike in the case of the neutral dynamics, the agreement here is only qualitative, and it is difficult to draw quantitative conclusions in light of the poor frequency-space resolution of the data. Moreover, as we discussed in the context of the neutral wave dispersion, we have no *a priori* justification for why the dispersion we have derived is applicable in upstream regions where ionization is non-negligible. Qualitatively, though, the ion waves do appear to convect downstream with finite phase velocity commensurate with the ion drift speed. Moreover, this convection of the oscillations in the downstream direction persists even in the upstream region with significant ionization, $z/L < 0.2$. This observation suggests that the ion density fluctuations—like the neutral waves—may represent waves that are modulated upstream of or at the ionization region

and propagate downstream at a phase velocity similar to the species drift speed. Although it ultimately is unsurprising that changes in ion density in response to the breathing mode appear as propagating waves downstream of the exit plane—this has been observed experimentally in the plume³² and can be explained simply by the convection of the plasma—the possibility that this modulation may also be a propagating wave in the ionization region itself is a departure from many numerical and theoretical treatments of the breathing mode. For example, many zero-dimensional models of the breathing mode like the traditional predator–prey description presume the instability as a standing wave contained in the entirety of the ionization and acceleration regions. Even higher-order simulations, which do show the convection of the waves downstream of the exit plane, seem to indicate that the ion waves do not propagate in the actual ionization zone.^{5,61} While ultimately explaining why these previous simulations may not have captured this propagating nature of the ion perturbations in the ionization region is beyond the scope of this investigation, we do remark that it is common in these simulations to impose a static electron mobility. Since the electron mobility is a critical factor that dictates both the electric field spatial distribution and the ion velocity profile, this static assumption could artificially limit the ability of simulations to resolve propagating ion quantities. In practice, as was shown experimentally in Ref. 24, the electron mobility can vary by orders of magnitude in the ionization region on the timescale of the breathing mode.

C. Measured evolution of wave amplitude

In Sec. V B, we showed through Eq. (13) that in regions of negligible ionization, the amplitudes of the neutral and ion waves would decay by following the changes in the respective steady-state densities. To compare this prediction with our measurements, we can compute the change in wave amplitude [the left sides of Eq. (13)] from our measurements and the theoretical change from the derivation of Sec. V B [the right sides of Eq. (13)]. For neutrals, the theoretical change in wave amplitude can further be approximated as $\tilde{n}_n^{-1} \partial \tilde{n}_n / \partial z \approx A_n / (dA_n / dz)$, where A_n is the neutral plume cross-sectional area (discussed in Sec. IV A). For comparison, we also show the measured profiles of the actual wave amplitudes, \tilde{n} and \tilde{n}_n . The curves are arbitrarily offset to match at the exit plane. The plots illustrate that the theoretical and measured profiles match well for both ions and neutrals—particularly in the downstream region where ionization is negligible, $z/L > 0.2$. This suggests that the change in wave amplitude may be explained in this region by the decay derived in Eq. (13).

To reinforce this point, we can directly compare effective measured decay rates to those predicted from our simplified theory. Just as a signal that decays exponentially in time has a growth rate with units s^{-1} , in which a negative value indicates a decrease, here we fit an exponential curve to the measured variations in amplitude to find a growth gradient with units m^{-1} . We find for ions that the mean measured value of this gradient is $-140 m^{-1}$ and the theoretical value from Eq. (13) $-128 m^{-1}$; for neutrals, these are -37 and $-43 m^{-1}$. Given that these values have a median uncertainty on the order of 41%, the measured gradients are consistent with those

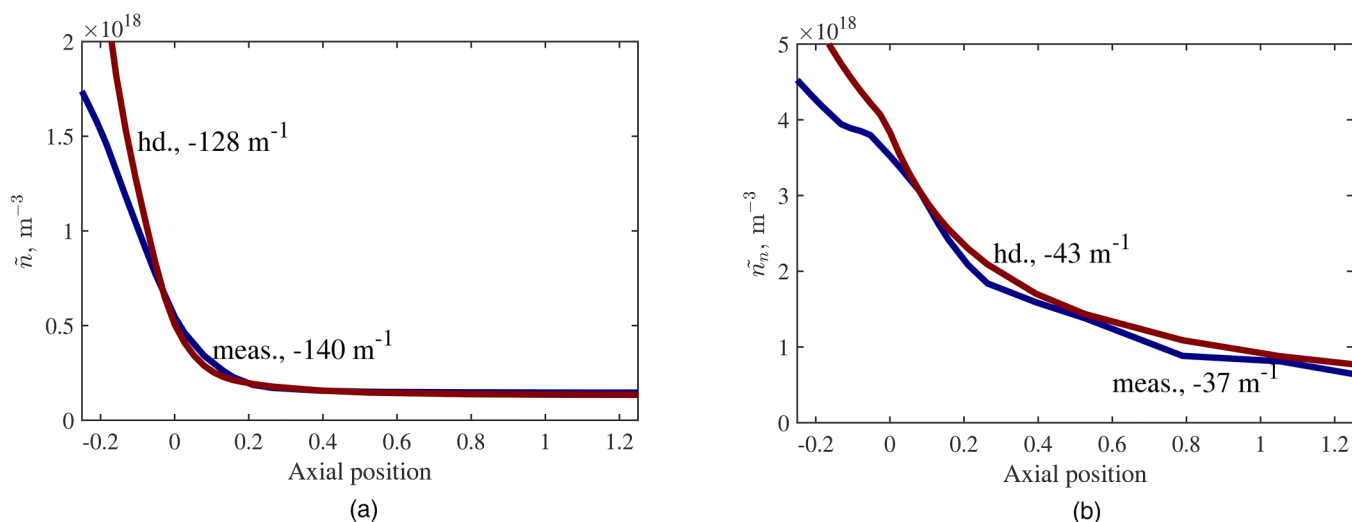


FIG. 11. The fluctuation strength for ion density (a) and neutral density (b), showing the measured profile (“meas.”) and the theoretical profile predicted from Eq. (13) (“hd.”).

theoretically due to changes in the background plasma and neutral densities.

With that said, we note from Fig. 11 that there is a discrepancy between the simple decay predicted from Eq. (13) and the measurement that occurs in both cases upstream of $z/L = 0$. Indeed, the wave amplitude decay appears to be less precipitous than is predicted from our simple model. This may suggest that there are other factors influencing the amplitude of the waves not captured in our analysis. This ultimately may not be surprising in light of the fact that the assumption of negligible ionization is violated in this upstream region. Indeed, the shallowness of the measured curves suggests a source of positive growth in this region. Isolating this contribution, however, would require a more detailed perturbation analysis of the source terms in the governing continuity equations. This, as we have discussed in the preceding, remains an open topic of inquiry.^{19,22,58,62}

This finding coupled with the dispersion relation results from Sec. V A suggests the following physical process: the ion and neutral waves correlated with the breathing mode exist upstream of or at the ionization region and propagate downstream at phase velocities commensurate with their drift species in the channel. As they propagate, the amplitudes decrease at a rate that can be explained largely by hydrodynamic effects, i.e., by the fact that the background properties are also decreasing. We qualify this interpretation, however, by noting we cannot speak to the damping or growth mechanisms outside the measurement domain. In particular, the behavior of electrons upstream of the ionization and acceleration regions has not been experimentally interrogated.

D. Discussion of possible driving mechanisms

In light of the trends we have observed, we qualitatively discuss in this section possible mechanisms that may contribute to the

formation of the neutral and ion waves. To this end, we recall that we thus far have identified from experimental data that neutral and ion drift waves exist in the channel; that they propagate downstream from a location upstream of or near the ionization region; and that the decay in amplitudes of both waves largely can be ascribed to the density gradients in the background plasma and neutral gas. Taken together, these trends support the hypothesis that the fluctuations begin propagating upstream of or at the ionization zone. If this is the case, there are at least two physically plausible explanations that may explain the formation of the waves. Both are based on the disparity in time scales of the propagation of the fluctuating quantities associated with the breathing mode. We carefully note here that these hypotheses are proposed in consideration of the trends in our data but are not proposed at the exclusion of the wide number of alternative numerical and analytical models that have been proposed to date (e.g., Refs. 22, 27, and 28). We do not have sufficient information to summarily dismiss or validate any theory yet for the energy source of the waves.

First, we consider the case in which the ion and neutral waves originate at the edge of the anode presheath. The anode presheath is defined here as the location where ion velocity stagnates before the anode sheath. This occurs in our setup near $z/L_{ch} = -0.4$, as shown in Fig. 5(a). Under these circumstances, we hypothesize that there is a coupling between ionization instabilities in the ionization zone and the presheath that produces the observed waves. In particular, the predator–prey action in the ionization zone periodically is correlated with a local rise in electron temperature. That is, it is evident from our results that the changes in local plasma density in the ionization region are negatively correlated with electron temperature (Fig. 8). We do not elaborate further here on the actual mechanism by which the temperature is correlated with density in the ionization region or the causality of these trends but this has been examined numerically in other studies (e.g., Ref. 27) and

observed experimentally (e.g., Ref. 24). These changes in T_e in the ionization region then are communicated “instantly” upstream as they convect with the energetic electrons. This physical interpretation is supported by the trends shown in Figs. 7 and 8 where we see that the electron temperature appears to vary globally, i.e., its fluctuations are dispersionless. The increased temperature at the presheath enhances ionization, locally increasing ion density and decreasing neutral density. These density modulations then propagate downstream with their respective species drifts [Eq. (12)] until they reach the ionization zone. This physical picture is supported qualitatively by Figs. 8(a) and 8(b). At this point, the decrease in neutral density and the increase in ion density at the ionization zone reinforce the predator–prey-like cycle occurring there, producing an increase in electron temperature that restarts the process.

This positive reinforcement ultimately is enabled by the disparity in the transit time of the ions from the upstream presheath to the ionization zone. This type of feedback is necessary for the spontaneous growth of the instability. Indeed, one of the reasons earlier theories for the breathing mode have failed to yield positive predicted growths (cf. Ref. 58 for an overview) is the absence of this type of destabilizing factor. With that said, we note that reinforcement is a necessary but not sufficient condition for growth—the wave must still draw energy from an external source. As has been proposed in previous studies (cf. Refs. 18, 22, and 27), presumably this energy source is related to the electron dynamics.

As a second possible mechanism, we consider the case where the ion wave originates at the presheath edge but the neutral wave originates at the anode. In this case, we make the admittedly strong assumption that the dispersion of Eq. (12) continues to apply in the upstream region—an assumption partially bolstered by the fact that our simplified dispersion relations ignoring ionization appear phenomenologically consistent with our measurements (Sec. V B). We presume then that just as the ions waves propagate downstream through the ionization and acceleration regions with the ion drift speed, they will propagate upstream toward the anode within the presheath. An increase in ion density at the presheath thus will lead to a propagating front returning to the anode. As this front reaches the anode, it recombines, leading to a local increase in neutral density. A similar process was discussed qualitatively in the simulation work by Smolyakov *et al.* in relation to the breathing mode.²² The increase in neutral density then propagates back downstream with the neutral drift speed. As these neutrals pass the presheath and enter the ionization zone, they lead to a local increase in ionization following a predator–prey-like cycle, driving in turn an increase in ion density. This increase in density propagates away from the stagnation point, restarting the process. If the time scale of ions transiting the sheath and returning downstream as neutrals matches that of the predator–prey action in the ionization zone, there will be positive feedback of this process, thus promoting the growth of the wave. With that said, we again note that to sustain the oscillation, net energy is likely extracted from the electrons. The phasing between perturbations is simply the destabilizing factor that allows for a net positive extraction of energy from this source.

Ultimately, without additional data farther upstream than what was acquired in the present study, we cannot determine which of these processes is occurring or whether all the conditions are met for them to exist in the first place. However, we propose

these hypotheses as plausible explanations in line with the observation of the perturbations in plasma properties that we have measured downstream. Deriving a fully predictive and first-principles explanation for the observed process is beyond the scope of this work, as we qualify in Sec. V E.

E. Qualification of results and discussion

The preceding experimental and theoretical analysis has served to inform a discussion of the nature of the measured waves in neutral and ion density that propagate at the breathing mode frequency. These waves appear to originate upstream of or at the traditional ionization region and thus the breathing mode may be initiated by the dynamics in this area. We have qualitatively discussed feedback mechanisms that could facilitate the development of these waves in Sec. V D. We remark here that our dispersion relation was only derived for the region downstream of the ionization zone where ionization is negligible, and although the agreement with dispersion appears to extend even upstream into the ionization region, our formulation does not explicitly include any growth terms. We thus have not offered a validated, quantifiable prediction for linear growth. We recognize then that the fact that these ion and neutral waves appear to originate upstream of or near the ionization zone does not necessarily mean that the energy source for the breathing mode is localized here.

To this point, previous studies have shown that the breathing mode growth may be attributed to a range of non-localized sources. For example, recent work by Romadanov *et al.* has suggested that the breathing mode may be a phenomenon originating near the anode where the time delay between backward streaming ions near the anode and neutral ionization serves to positively reinforce and promote the growth of the wave.²¹ This is qualitatively consistent with our experimental observations. Alternatively, the Hall thruster discharge is an inherently global plasma where the electron dynamics are communicated almost instantaneously compared to the time scale of the breathing mode oscillations [Fig. 8(e)]. The waves thus may “appear” to originate in the upstream portion of the channel but the actual energy source is from a species that is born downstream of the ionization region. For example, the electron heating dynamics in the main discharge¹⁸ and at the boundary conditions²⁷ may play a critical role in the local energy balance, which, in turn, impacts the onset of this oscillation. In summary, even though we observe waves propagating at the species drift speeds that themselves appear to originate upstream, we cannot rule out the possibility that the actual dynamics that govern the growth of the breathing mode as a whole originates at other locations in the thruster. To address the question of what energy source drives these dynamics, experimental data at time scales much shorter than the breathing mode and in more varied locations—like very close to the cathode and anode—must be taken to more precisely examine the electron dynamics involved in this instability. This information could help reveal whether energy from electrons originating in the ionization zone is driving the breathing mode or whether the energy is principally sourced elsewhere.

VI. CONCLUSIONS

In this article, we have experimentally investigated the Hall thruster breathing mode using a minimally invasive diagnostic approach. We were able to measure and calculate a wide range of time-resolved ion, neutral, and electron properties. After making these measurements throughout an entire breathing period and over a large axial domain, we made use of Fourier analysis to track the amplitude and phase of ion and neutral fluctuations.

From these results, we examined several aspects of the ion and neutral waves correlated with the breathing mode, including their dispersion, axial change in amplitude, and possible explanations for their origin. First, we showed that the existence of distinct ion and neutral drift waves satisfies 1D fluid continuity. We then demonstrated experimentally that fluctuations in neutral and ion density are representative of waves that propagate with phase velocities commensurate with the species drift speeds.

We next investigated the change in amplitude of the observed waves. We found that not only do the waves exist upstream of the ionization region but they decay continuously throughout the measurement domain. Further, this decay is consistent with the fact that the waves are propagating down density gradients resulting from the accelerating ion beam and expanding neutral plume. This provides more evidence that our simple dispersion relation describing concurrent propagation of ion and neutral waves is consistent with the experimental data.

Finally, using our conclusions about the dispersion and decay of the measured ion and neutral waves, we discussed possible mechanisms governing their onset. We focused on two possibilities: the coupling of ionization instabilities as the edge of the anode pre-sheath and the traditional ionization zone, and the periodic recombination of ions on the anode coupling to an ionization instability. However, while we have noted that these mechanisms would be consistent with our findings, we qualified these hypotheses with the understanding that our measurements did not have sufficient time resolution or spatial access to validate them directly.

In summary, the measurements of the breathing mode we have presented here have yielded new and unprecedented experimental insight into the dynamics of this type of oscillation. While we have started to discuss the physical implications of these results in this work, it is our hope that these types of localized, non-invasive measurements will provide the necessary data for validating existing models or yielding new physically inspired ones. Armed with such a result, we may be able to realize the ultimate goal of predicting—and potentially controlling—this nearly ubiquitous oscillation in Hall thrusters.

ACKNOWLEDGMENTS

The authors would like to acknowledge the technical assistance of Eric Viges in maintaining the vacuum facility during these experiments.

APPENDIX A: NON-PHYSICAL IONIZATION FREQUENCIES

The ionization frequency cannot be negative on physical grounds, yet its calculation with IBIS via Eq. (3a) can still yield

negative values. This is largely a result of the numerical approach used in solving the system of equations in Eq. (1). As shown in Eq. (3a), in a time-averaged sense, f_{iz} is calculated as the ratio of two quantities: $N - \overline{u_i}dD/dz$ and D . It is sufficient to show that, if both of these quantities exhibit zero crossings, even slight noise in the measured moments may lead to erratic sign changes in f_{iz} . When f_{iz} is very small and thus its uncertainty relatively high, then, it will become prone to dipping negative.

As a simple example, the case of monoenergetic ion velocity moments is considered, i.e., $\overline{u_i^j} = \overline{u_i^j}$ for all moments of order j . With this approximation,

$$f_{iz} \approx \frac{3u_i^3 \frac{du_i}{dz} - u_i \frac{du_i^3}{dz}}{3u_i^3}, \quad (\text{A1})$$

such that $f_{iz} \approx 0$ when u_i has no error. If u_i has some uncertainty ϵ , then to first order

$$f_{iz} \approx \frac{2\epsilon \frac{du_i}{dz}}{u_i + \epsilon}. \quad (\text{A2})$$

For ϵ randomly distributed about zero, this means f_{iz} may be as low as $-2|\epsilon|(du_i/dz)/(u_i - |\epsilon|)$. For a typical $du_i/dz \sim 10^6 \text{ s}^{-1}$, an uncertainty of only 5% may produce f_{iz} as low as nearly -11 kHz . In this way, the inference of negative ionization frequencies is a numerical artifact and not representative of an unphysical assumption of the IBIS method.

APPENDIX B: PHASE DETERMINATION

Since the ion velocity profile varies over a breathing cycle [Fig. 8(c)], it is possible that the fluctuations in ion quantities at a given location are not perfectly sinusoidal and thus the method for determining phase described in Sec. IV B (“FFT”) is inaccurate.

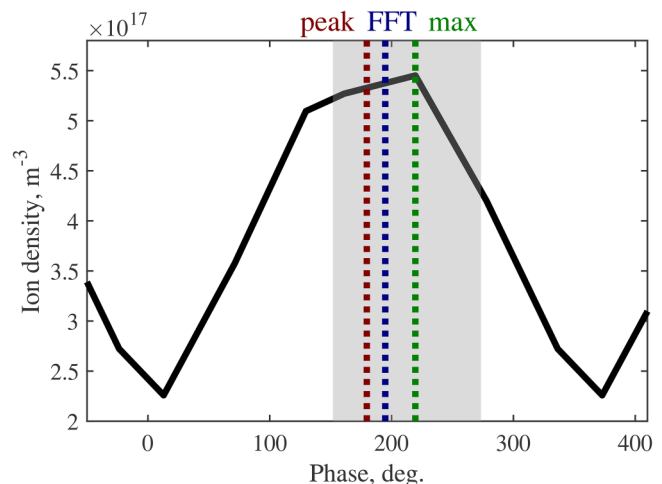


FIG. 12. A sample of the phase determination methods used in this study, including a total uncertainty region of the phase based on all the methods.

Further, although the Nyquist criterion is satisfied with our TRLIF measurements (Sec. III A), the frequency–space resolution of θ is expected to be poor: $\pm 27^\circ$. Together, these factors suggest that determining θ with the FFT method may not be accurate. Alternatively, we can estimate the phase from the propagation of wave crests. In this study, we established a lower limit for phase speed using this method simply by tracking the phase at which n is maximum as a function of axial location (“max”). More rigorously, given that peaks in \tilde{n} occur when $\partial\tilde{n}/\partial t = 0$, we can define an instantaneous phase as that at which $\mathcal{F}(\partial\tilde{n}/\partial t) = i\omega\mathcal{F}(\tilde{n})$ is nearly constant (“peak”). Specifically, this is accomplished by numerically minimizing the variance of $\Re[i e^{i\theta}\omega\mathcal{F}(\tilde{n})]$ at each axial location for a local phase θ . As an example, Fig. 12 shows a comparison of the different phase determination methods for the ion density signal at $z/L_{ch} = -0.03$. Notice that “max” coincides with the greatest n value at this location, whereas “peak” and “FFT” are closer to the intuitive center of the waveform.

DATA AVAILABILITY

The data that support the findings of this study are available from the corresponding author upon reasonable request.

REFERENCES

- D. Y. Oh, S. Collins, D. Goebel, B. Hart, G. Lantoine, S. Snyder, G. Whiffen, L. Elkins-Tanton, P. Lord, Z. Pirkl, and L. Rotlisburger, “Development of the psyche mission for NASA’s discovery program,” in *35th International Electric Propulsion Conference* (ERPS, Atlanta, GA, 2017).
- J. Zubair, “Development of a 12.5 kW Hall thruster for the advanced electric propulsion system,” in *AIAA Propulsion and Energy 2020 Forum* (American Institute of Aeronautics and Astronautics, 2020).
- E. Y. Choueri, “Plasma oscillations in Hall thrusters,” *Phys. Plasmas* **8**, 1411–1426 (2001).
- J. Fife, M. Martinez-Sanchez, and J. Szabo, “A numerical study of low-frequency discharge oscillations in Hall thrusters,” in *33rd AIAA/ASME/SAE/ASEE Joint Propulsion Conference & Exhibit* (American Institute of Aeronautics and Astronautics, 1997).
- J. P. Boeuf and L. Garrigues, “Low frequency oscillations in a stationary plasma thruster,” *J. Appl. Phys.* **84**, 3541–3554 (1998).
- R. B. Lobbia, “A time-resolved investigation of the Hall thruster breathing mode,” Ph.D. thesis (University of Michigan, Ann Arbor, MI, 2010).
- M. J. Sekerak, A. D. Gallimore, D. L. Brown, R. R. Hofer, and J. E. Polk, “Mode transitions in Hall-effect thrusters induced by variable magnetic field strength,” *J. Propul. Power* **32**, 903–917 (2016).
- K. Polzin, E. Sooby, Y. Raitses, E. Merino, and N. Fisch, “Discharge oscillations in a permanent magnet cylindrical Hall-effect thruster,” in *31st International Electric Propulsion Conference* (ERPS, Ann Arbor, MI, 2009).
- D. P. Schmidt, N. B. Meezan, W. A. Hargus, and M. A. Cappelli, “A low-power, linear-geometry Hall plasma source with an open electron-drift,” *Plasma Sources Sci. Technol.* **9**, 68–76 (2000).
- C. Garner, J. Brophy, S. Semenko, V. Garkusha, S. Tverdokhlebov, and C. Marrese, “Experimental evaluation of Russian anode layer thrusters,” in *30th Joint Propulsion Conference and Exhibit* (American Institute of Aeronautics and Astronautics, Indianapolis, IN, 1994).
- R. Conversano, “Low-power magnetically shielded Hall thrusters,” Ph.D. thesis (University of California, Los Angeles, 2015).
- M. J. Sekerak, B. Longmier, A. Gallimore, W. Huang, H. Kamhawi, R. R. Hofer, B. Jorns, and J. E. Polk, “Mode transitions in magnetically shielded Hall effect thrusters,” in *50th AIAA/ASME/SAE/ASEE Joint Propulsion Conference* (American Institute of Aeronautics and Astronautics, Cleveland, OH, 2014).
- S. Mazouffre, S. Tsikata, and J. Vaudolon, “Development and experimental characterization of a wall-less Hall thruster,” *J. Appl. Phys.* **116**, 243302 (2014).
- B. Karadag, S. Cho, and I. Funaki, “Thrust performance, propellant ionization, and thruster erosion of an external discharge plasma thruster,” *J. Appl. Phys.* **123**, 153302 (2018).
- Y. Yang, X. Zhou, J. X. Liu, and A. Anders, “Evidence for breathing modes in direct current, pulsed, and high power impulse magnetron sputtering plasmas,” *Appl. Phys. Lett.* **108**, 034101 (2016).
- A. Gallimore, M. Reichenbacher, C. Marrese, S.-W. Kim, and J. Foster, “Preliminary characterization of a low power end-Hall thruster,” in *30th Joint Propulsion Conference and Exhibit* (American Institute of Aeronautics and Astronautics, Indianapolis, IN, 1994).
- S. Chable and F. Rogier, “Numerical investigation and modeling of stationary plasma thruster low frequency oscillations,” *Phys. Plasmas* **12**, 033504 (2005).
- S. Barral and E. Ahedo, “Low-frequency model of breathing oscillations in Hall discharges,” *Phys. Rev. E* **79**, 046401 (2009).
- K. Hara, M. J. Sekerak, I. D. Boyd, and A. D. Gallimore, “Perturbation analysis of ionization oscillations in Hall effect thrusters,” *Phys. Plasmas* **21**, 122103 (2014).
- O. Koshkarov, A. I. Smolyakov, I. V. Romadanov, O. Chapurin, M. V. Umansky, Y. Raitses, and I. D. Kaganovich, “Current flow instability and nonlinear structures in dissipative two-fluid plasmas,” *Phys. Plasmas* **25**, 011604 (2018).
- I. V. Romadanov, A. I. Smolyakov, E. A. Sorokina, V. V. Andreev, and N. A. Marusov, “Stability of ion flow and role of boundary conditions in a simplified model of the $E \times B$ plasma accelerator with a uniform electron mobility,” *Plasma Phys. Rep.* **46**, 363–373 (2020).
- A. Smolyakov, O. Chapurin, I. Romadanov, Y. Raitses, and I. Kaganovich, “Stationary profiles and axial mode oscillations in Hall thrusters,” in *AIAA Propulsion and Energy 2019 Forum* (American Institute of Aeronautics and Astronautics, 2019).
- S. Tsikata, A. Heron, and C. Honore, “Oscillatory discharge behavior in Hall thrusters: Relationships between the discharge current, electric field and micro-turbulence,” in *IEPC-2017-443* (ERPS, Atlanta, GA, 2017).
- E. T. Dale and B. A. Jorns, “Non-invasive time-resolved measurements of anomalous collision frequency in a Hall thruster,” *Phys. Plasmas* **26**, 013516 (2019).
- K. Hara and I. G. Mikellides, *Characterization of Low Frequency Ionization Oscillations in Hall Thrusters Using a One-Dimensional Fluid Model* (American Institute of Aeronautics and Astronautics, Cincinnati, OH, 2018).
- I. Romadanov, Y. Raitses, and A. Smolyakov, “Hall thruster operation with externally driven breathing mode oscillations,” *Plasma Sources Sci. Technol.* **27**, 094006 (2018).
- K. Hara, M. J. Sekerak, I. D. Boyd, and A. D. Gallimore, “Mode transition of a Hall thruster discharge plasma,” *J. Appl. Phys.* **115**, 203304 (2014).
- S. Barral and Z. Peradzyński, “Ionization oscillations in Hall accelerators,” *Phys. Plasmas* **17**, 014505 (2010).
- E. T. Dale and B. Jorns, “Frequency scaling of the Hall thruster breathing mode,” in *AIAA Propulsion and Energy 2019 Forum*, AIAA Propulsion and Energy Forum (American Institute of Aeronautics and Astronautics, Indianapolis, IN, 2019).
- M. S. McDonald and A. D. Gallimore, “Comparison of breathing and spoke mode strength in the H6 Hall thruster using high speed imaging,” in *33rd International Electric Propulsion Conference* (ERPS, Washington DC, 2013).
- M. S. McDonald, C. K. Bellant, B. A. S. Pierre, and A. D. Gallimore, “Measurement of cross-field electron current in a Hall thruster due to rotating spoke instabilities,” in *47th AIAA/ASME/SAE/ASEE Joint Propulsion Conference & Exhibit* (American Institute of Aeronautics and Astronautics, San Diego, CA, 2011).
- R. B. Lobbia and A. D. Gallimore, “High-speed dual Langmuir probe,” *Rev. Sci. Instrum.* **81**, 073503 (2010).

- ³³M. Sekerak, M. McDonald, R. Hofer, and A. Gallimore, "Hall thruster plume measurements from high-speed dual Langmuir probes with ion saturation reference," in *2013 IEEE Aerospace Conference* (IEEE, 2013), pp. 1–16.
- ³⁴M. J. Sekerak, "Plasma oscillations and operational modes in Hall effect thrusters," Ph.D. thesis (National Aeronautics and Space Administration, 2014).
- ³⁵C. R. Mullins, C. C. Farnell, C. C. Farnell, R. A. Martinez, D. Liu, R. D. Branam, and J. D. Williams, "Non-invasive Hall current distribution measurement in a Hall effect thruster," *Rev. Sci. Instrum.* **88**, 013507 (2017).
- ³⁶B. Jorns, D. M. Goebel, and R. R. Hofer, "Plasma perturbations in high-speed probing of Hall thruster discharge chambers: Quantification and mitigation," in *51st AIAA/SAE/ASEE Joint Propulsion Conference* (American Institute of Aeronautics and Astronautics, Orlando, FL, 2015).
- ³⁷L. Grimaud, A. Petin, J. Vaudolon, and S. Mazouffre, "Perturbations induced by electrostatic probe in the discharge of Hall thrusters," *Rev. Sci. Instrum.* **87**, 043506 (2016).
- ³⁸E. Viges, B. Jorns, A. Gallimore, and J. Sheehan, "University of Michigan's upgraded large vacuum test facility," in *36th International Electric Propulsion Conference* (ERPS, Vienna, 2019).
- ³⁹R. Hofer, S. Cusson, R. Lobbia, and A. Gallimore, "The H9 magnetically shielded Hall thruster," in *35th International Electric Propulsion Conference, IEPC-2017-232* (ERPS, 2017).
- ⁴⁰S. Cusson, R. Hofer, R. Lobbia, B. Jorns, and A. Gallimore, "Performance of the H9 magnetically shielded Hall thrusters," in *35th International Electric Propulsion Conference, IEPC-2017-239* (ERPS, 2017).
- ⁴¹J. W. Dankanich, M. Walker, M. W. Swiatek, and J. T. Yim, "Recommended practice for pressure measurement and calculation of effective pumping speed in electric propulsion testing," *J. Propul. Power* **33**, 668–680 (2017).
- ⁴²P. Y. Peterson, H. Kamhawi, W. Huang, G. Williams, J. H. Gilland, J. Yim, R. R. Hofer, and D. A. Herman, "NASA's HERMeS Hall thruster electrical configuration characterization," in *52nd AIAA/SAE/ASEE Joint Propulsion Conference* (American Institute of Aeronautics and Astronautics, 2016).
- ⁴³E. T. Dale, "Investigation of the Hall thruster breathing mode," Ph.D. thesis (University of Michigan, Ann Arbor, MI, 2019).
- ⁴⁴N. A. MacDonald, M. A. Cappelli, and W. A. Hargus, "Time-synchronized continuous wave laser-induced fluorescence on an oscillatory xenon discharge," *Rev. Sci. Instrum.* **83**, 113506 (2012).
- ⁴⁵J. Perez-Luna, G. J. M. Hagelaar, L. Garrigues, and J. P. Boeuf, "Method to obtain the electric field and the ionization frequency from laser induced fluorescence measurements," *Plasma Sources Sci. Technol.* **18**, 034008 (2009).
- ⁴⁶L. L. Su, A. R. Vazsonyi, and B. Jorns, "Performance of a 9-kW magnetically shielded Hall thruster with krypton," in *AIAA Propulsion and Energy 2020 Forum* (American Institute of Aeronautics and Astronautics, 2020).
- ⁴⁷D. Goebel and I. Katz, *Fundamentals of Electric Propulsion: Ion and Hall Thrusters* (John Wiley & Sons, 2008), Vol. 1.
- ⁴⁸R. Hofer, D. Goebel, I. Mikellides, and I. Katz, "Design of a laboratory Hall thruster with magnetically shielded channel walls, phase II: Experiments," in *48th AIAA/ASME/SAE/ASEE Joint Propulsion Conference & Exhibit* (American Institute of Aeronautics and Astronautics, Atlanta, GA, 2012).
- ⁴⁹S. Mazouffre, G. Bourgeois, L. Garrigues, and E. Pawelec, "A comprehensive study on the atom flow in the cross-field discharge of a Hall thruster," *J. Phys. D: Appl. Phys.* **44**, 105203 (2011).
- ⁵⁰W. Huang, A. D. Gallimore, and R. R. Hofer, "Neutral flow evolution in a six-kilowatt Hall thruster," *J. Propul. Power* **27**, 553–563 (2011).
- ⁵¹L. V. S. A. Barral and S. E. Ahedo, "Numerical investigation of low-frequency longitudinal oscillations in Hall thrusters," in *29th International Electric Propulsion Conference* (ERPS, Princeton, NJ, 2005).
- ⁵²S. Mazouffre, D. Gawron, and N. Sadeghi, "A time-resolved laser induced fluorescence study on the ion velocity distribution function in a Hall thruster after a fast current disruption," *Phys. Plasmas* **16**, 043504 (2009).
- ⁵³A. Diallo, S. Keller, Y. Shi, Y. Raitses, and S. Mazouffre, "Time-resolved ion velocity distribution in a cylindrical Hall thruster: Heterodyne-based experiment and modeling," *Rev. Sci. Instrum.* **86**, 033506 (2015).
- ⁵⁴A. Lucca Fabris, C. V. Young, and M. A. Cappelli, "Time-resolved laser-induced fluorescence measurement of ion and neutral dynamics in a Hall thruster during ionization oscillations," *J. Appl. Phys.* **118**, 233301 (2015).
- ⁵⁵C. J. Durot, "Development of a time-resolved laser-induced fluorescence technique for nonperiodic oscillations," Ph.D. thesis (University of Michigan, Ann Arbor, MI, 2016).
- ⁵⁶S. E. Cusson, E. T. Dale, B. A. Jorns, and A. D. Gallimore, "Acceleration region dynamics in a magnetically shielded Hall thruster," *Phys. Plasmas* **26**, 023506 (2019).
- ⁵⁷B. Efron, "Bootstrap methods: Another look at the jackknife," *Ann. Stat.* **7**, 1–26 (1979).
- ⁵⁸E. T. Dale, B. Jorns, and K. Hara, *Numerical Investigation of the Stability Criteria for the Breathing Mode in Hall Effect Thrusters* (ERPS, Atlanta, GA, 2017).
- ⁵⁹P. Coche and L. Garrigues, "A two-dimensional (azimuthal-axial) particle-in-cell model of a Hall thruster," *Phys. Plasmas* **21**, 023503 (2014).
- ⁶⁰F. Taccogna and L. Garrigues, "Latest progress in Hall thrusters plasma modeling," *Rev. Mod. Plasma Phys.* **3**, 295 (2019).
- ⁶¹J. C. Adam, A. Héron, and G. Laval, "Study of stationary plasma thrusters using two-dimensional fully kinetic simulations," *Phys. Plasmas* **11**, 295–305 (2004).
- ⁶²S. Barral and E. Ahedo, "Theoretical study of the breathing mode in hall thrusters," in *42nd AIAA/ASME/SAE/ASEE Joint Propulsion Conference & Exhibit* (American Institute of Aeronautics and Astronautics, Sacramento, CA, 2006).